Electronic Supplementary Material (ESI) for Chemical Science.

Zinc Ion Interactions in a Two-Dimensional Covalent Organic Framework based Aqueous Zinc Ion Battery

Abdul Khayum M, [1, 2] Meena Ghosh, [1, 2] Vidyanand Vijayakumar, [1, 2] Arjun Halder, [1, 2] Maryam Nurhuda, [3] Sushil Kumar, [2] Matthew Addicoat, [3] Sreekumar Kurungot, [1, 2*] Rahul Banerjee [4*]

[1] Academy of Scientific and Innovative Research (AcSIR). Ghaziabad, Uttar Pradesh 201002, India.

[2]Physical/ Materials Chemistry Division, CSIR-National Chemical Laboratory, Dr. Homi Bhabha Road, Pune-411008, India.

[3]School of Science and Technology, Nottingham Trent University, Clifton Lane, NG11 8NS Nottingham, United Kingdom.

[4]Department of Chemical Sciences, Indian Institute of Science Education and Research, Kolkata, Mohanpur 741246, India.

S-1: General information

General remarks: *1,3,5*- triformylphloroglucinol was synthesized by the reference of reported literatures.[1, 2] All other chemicals were commercially available and used as such without any further purification. 2,5-diaminohydroquinone dihydrochloride was purchased from Sigma Aldrich. Wide-angle X-ray diffraction (WAXD) patterns were recorded on a Rigaku, MicroMax-007HF with high-intensity Microfocus rotating anode X-ray generator. All samples were recorded in the 2θ range of 2–40 degrees and data was collected with the help of Control Win software. A Rigaku, R-axis IV++ detector was employed in wide-angle experiments. The radiation used as CuK (1.54 Å) with a Ni filter, and the data collection was carried out using an aluminium holder. Fourier transform infrared (FT-IR) spectra were taken on a Bruker Optics ALPHA-E spectrometer with a universal Zn-Se ATR (attenuated total reflection) accessory in the 600-4000 cm^{-1} region or using a Diamond ATR (Golden Gate). Thermo gravimetric analyses (TGA) were carried out on a TG50 analyzer (Mettler-Toledo) or a SDT Q600 TG-DTA analyzer under N_2 atmosphere at a heating rate of 20 ºC min^{-1} within a temperature range of 50-900° C. Low-pressure volumetric N_2 gas adsorption measurements were performed on activated COF at 77 K, maintained by a liquid nitrogen bath, with pressures ranging from 0 to 760 Torr (1 bar) on a Quantachrome, Quadrasorb automatic volumetric instrument. SEM images were obtained with a Zeiss DSM 950 scanning electron microscope and FEI, QUANTA 200 3D Scanning Electron Microscope with tungsten filament as electron source operated at 10 kV. The samples were sputtered with Au (nano-sized film) prior to imaging by a SCD 040 Balzers Union. TEM images were recorded using FEI Tecnai G2 F20 X-TWIN TEM at an accelerating voltage of 200 kV. The TEM Samples were prepared by the **HqTp** COF dispersed in acetonitrile solvent by 20 minute sonication and then drop casted on copper grids TEM Window (TED PELLA, INC. 200 mesh). ^{13}C CP MAS Solid state NMR (SSNMR) spectra were taken in a Bruker 300 MHzNMR spectrometer. X-ray photoelectron spectroscopy (XPS) measurement was carried out by a VG Microtech, model ESCA 3000 instrument equipped with ion gun (EX-05) for cleaning the surface. All electrochemical analysis include cyclic voltammetry (CV), impedance measurements (Electrochemical Impedance Spectroscopic [EIS]) investigation was performed from 10^6 to 0.01 Hz frequency against the open circuit potential with a sinus amplitude of 10 mV [Vrms = 7.07mV]) and galvanostatic charge/discharge measurements (GCDC) were carried out

using a Bio-LogicSP-300 PG Stat instrument. Electrochemical data were analyzed in EC-Lab software **V10.19.**

Atomic positions and cell sizes of the **HqTp** COF layers were optimized using the Self-Consistent-Charge Density-Functional Tight-Binding (SCC-DFTB) method, including Lennard-Jones dispersion. C, N, O, H atoms were described using the mio-0-1 parameter set [DOI: 10.1103/PhysRevB.58.7260], and Zn atoms were described using the znorg-0-1 parameters [DOI:10.1021/ct800455a].The monolayer, eclipsed (AA), slipped-AA and staggered (AB) stacking were considered. To determine the positions of the Zinc atoms, 6 Zn atoms per unit cell were randomly placed in the previously optimized AA and slipped-AA COF models and optimized. From 50 optimizations, the lowest energy structure of Zn-**HqTp** was kept.

S-2: Synthetic procedure

HqTp COF: *2, 5*-diaminohydroquinone dihydrochloride (**Hq**, 0.6 mmol) and *p*-toluenesulphonic acid (**PTSA,** 3 mmol) are thoroughly mixed at room temperature and 50 µl of water is added to the system. To the homogeneous mixture *1,3,5*-triformylphloroglucinol (**Tp**, 0.4 mmol) is added and again mixed vigorously for 10 minutes. The obtained black coloured paste is heated to 90°C for 24 hours under closed condition. Later, the COF after the thermal treatment is washed by the following order with water (3 times), *N,N*-dimethylacetamide (3 times), water (3 times) and acetone (3 times) (Isolated yield: >80%).

PaTp COF: p-Phenylenediamine (**Pa**, 0.6 mmol) and *p*-toluenesulphonic acid (**PTSA,** 3 mmol) are thoroughly mixed at room temperature and 50 µl of water is added to the system. To the homogeneous mixture *1,3,5*-triformylphloroglucinol (**Tp**, 0.4 mmol) is added and again mixed vigorously for 10 minutes. The obtained paste is heated to 90°C for 24 hours under closed condition. Later, the COF after the thermal treatment is washed by the following order with water (3 times), *N, N*-dimethylacetamide (3 times), water (3 times) and acetone (3 times) (Isolated yield: >90%).

S-3: Structural modeling, PXRD and DFTB

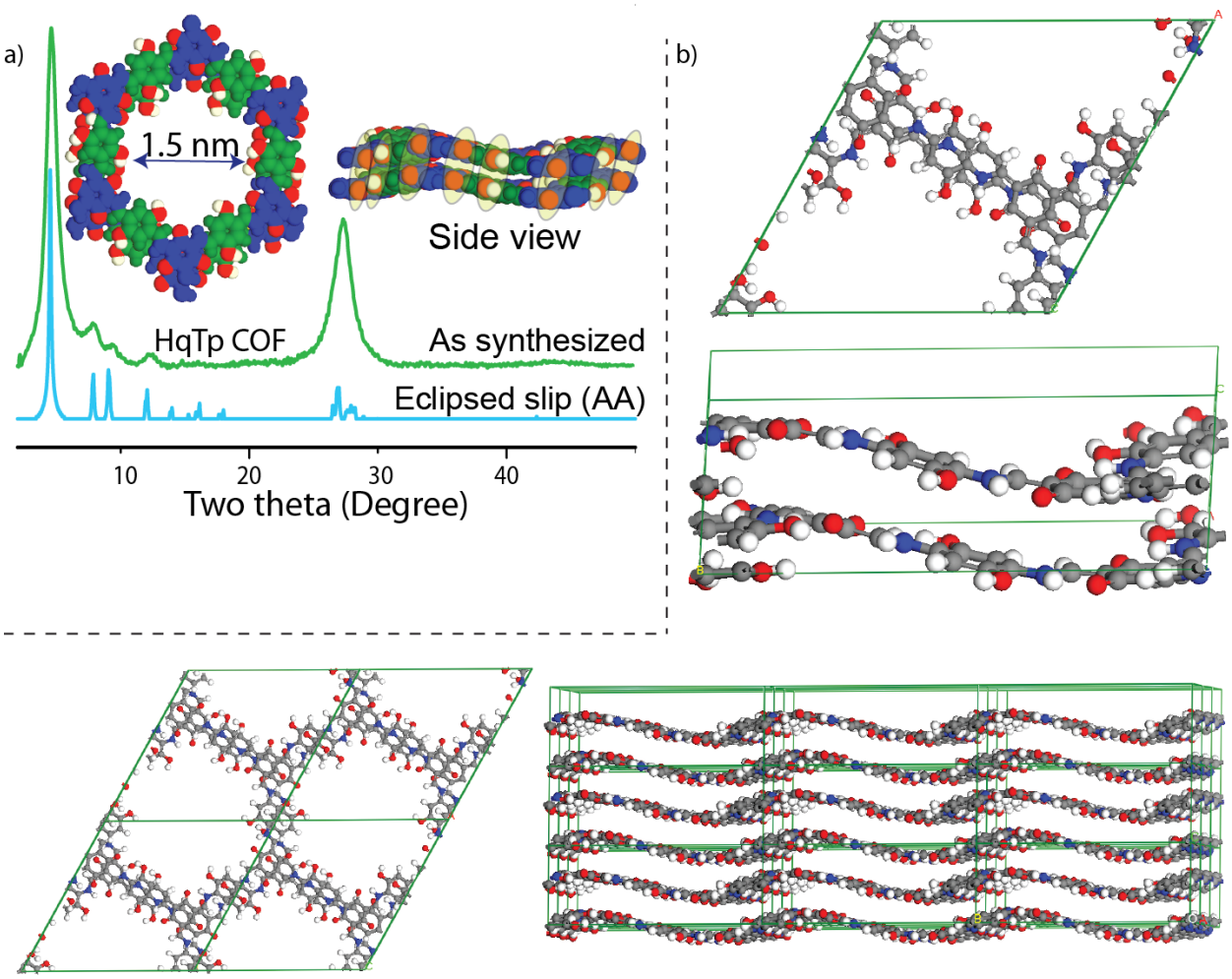

Figure S1: The structural modeling of **HqTp** COF. a) The experimental PXRD of **HqTp** matches with the eclipsed slip AA model. b) The unit cell of **HqTp** in front and side views.

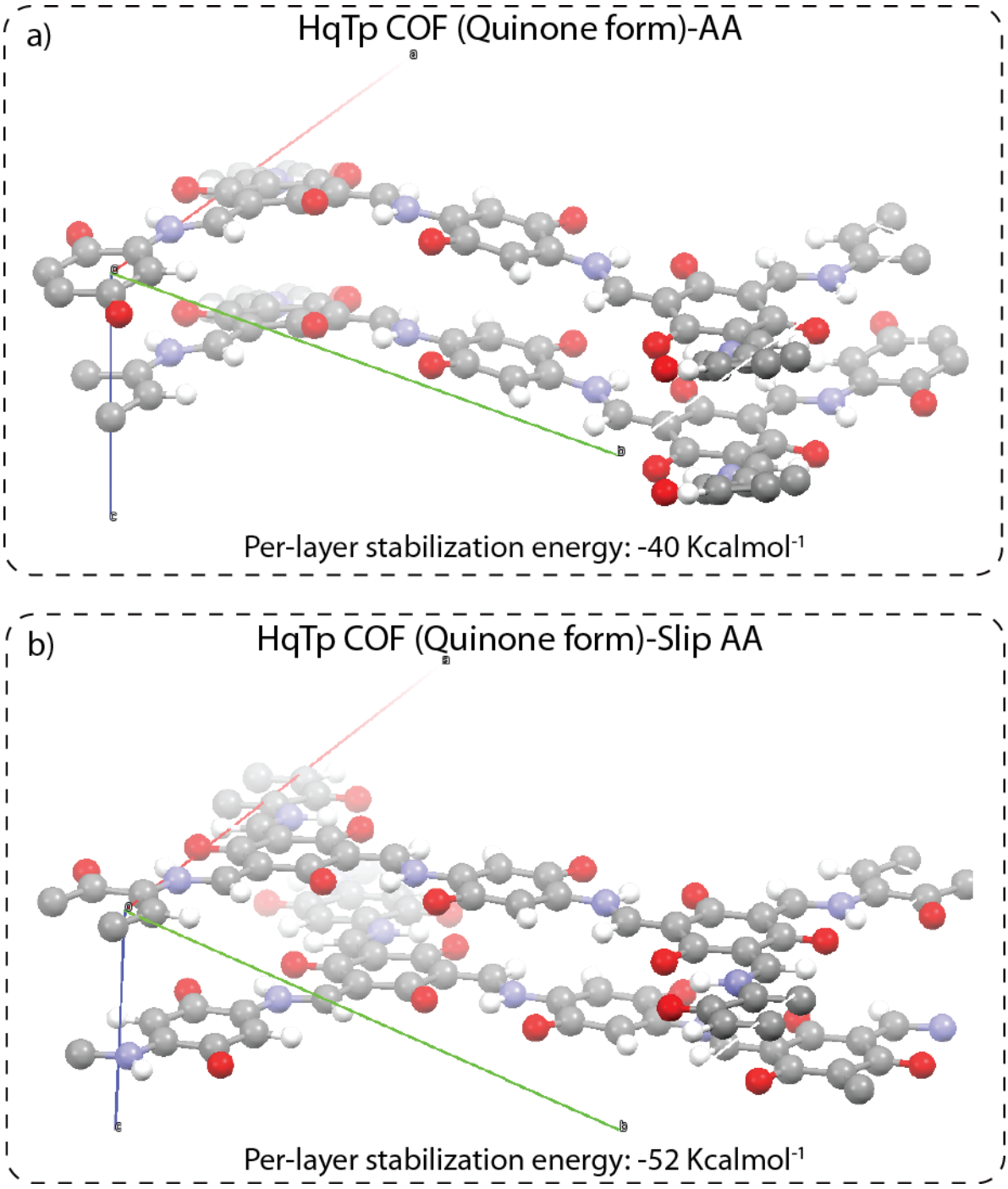

Figure S2: The unit cells of **HqTp** in quinone form in a) AA and b) slip AA stacked models with the perlayer stabilization energy. It indicates the slip form exhibits more stabilization energy compared to the AA stacked.

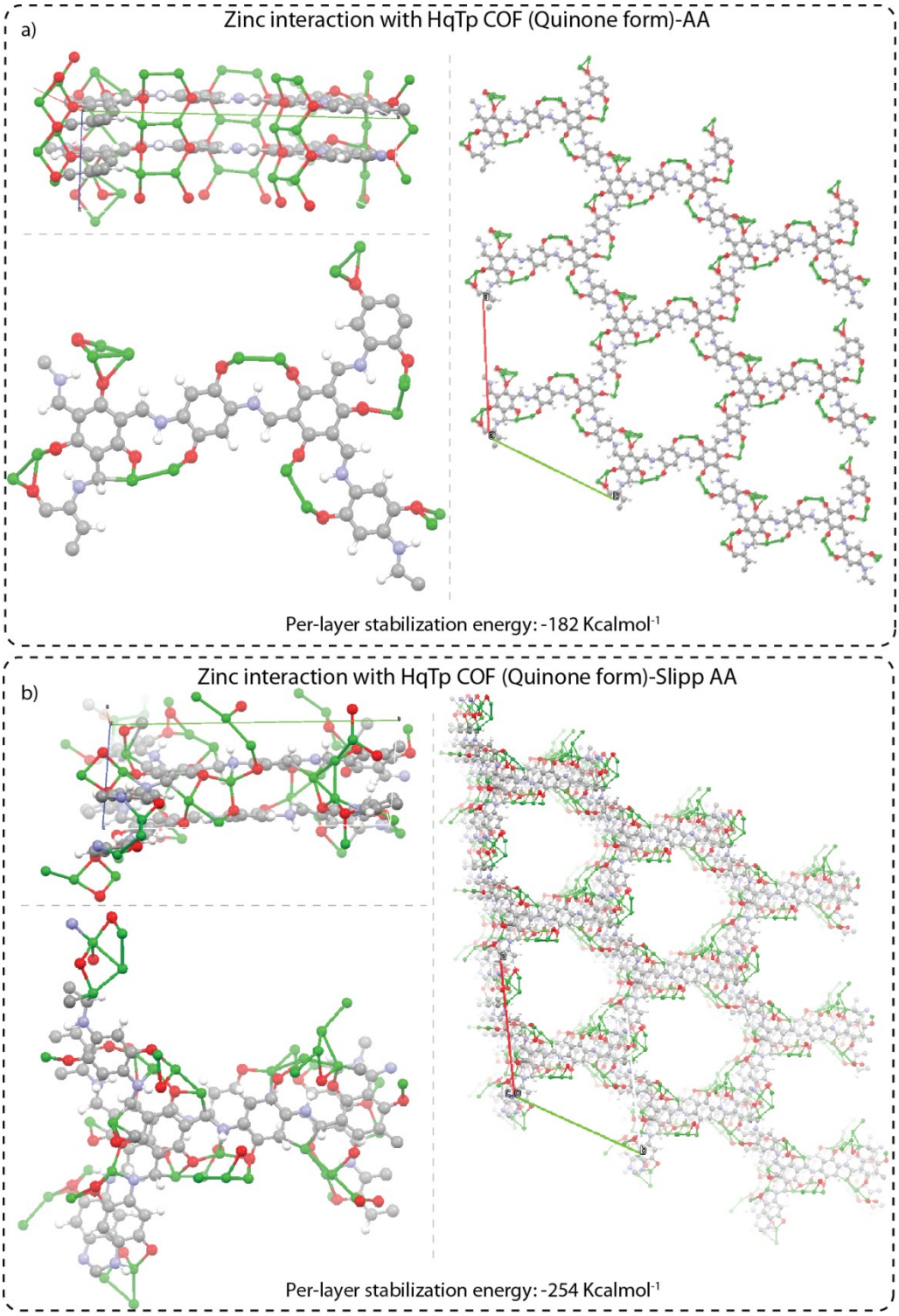

Figure S3: The DFTB models of Zinc interaction with a) AA stacked and b) slip AA stacked **HqTp** COF. The Zinc interaction with slip form of COF provides a large enhancement in energy stabilization compared to the simple AA stacked form of COF.

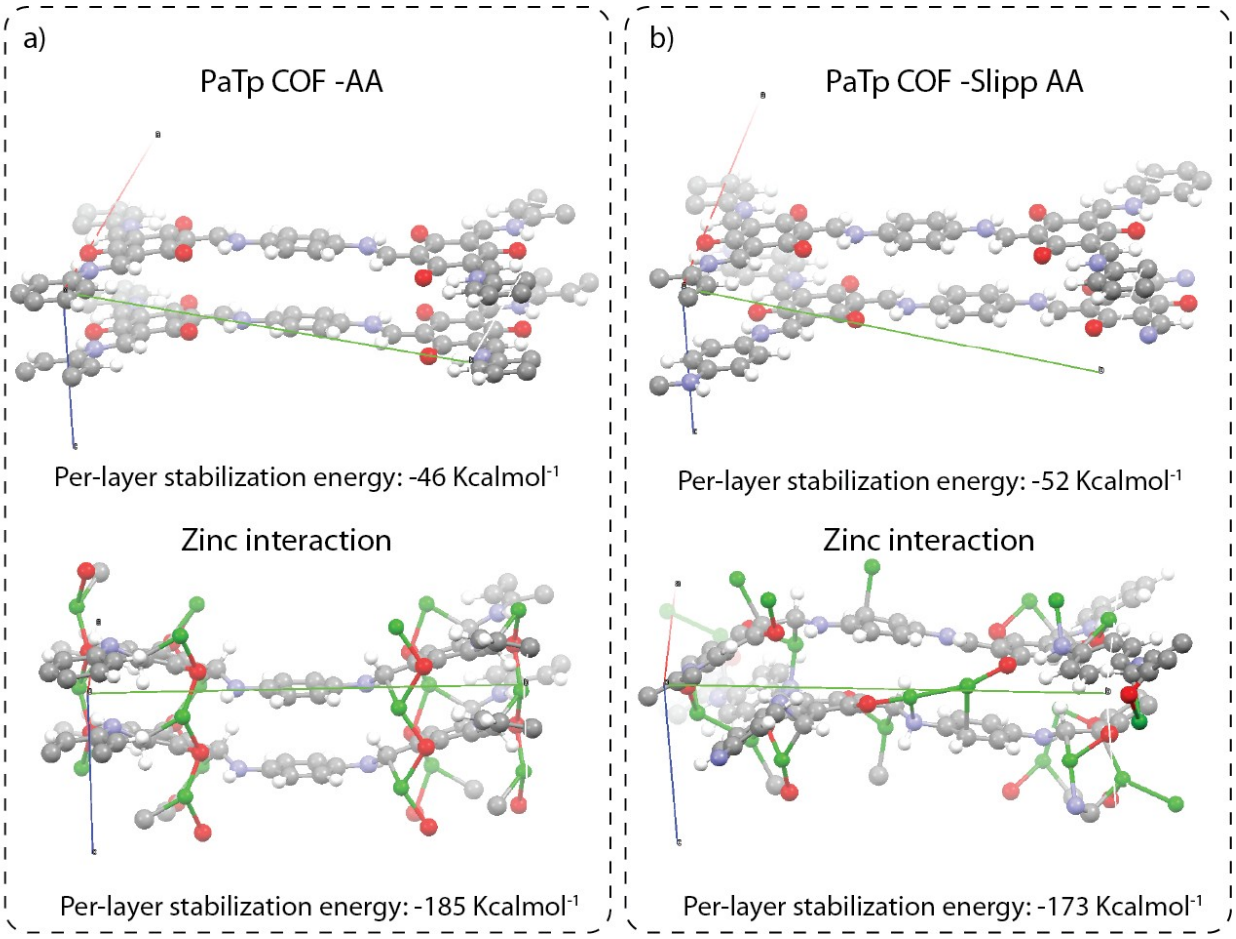

Figure S4: The DFTB models of Zinc interaction with a) AA stacked and b) slip AA stacked **PaTp** COF. Due to the less number of the active sites, the number of zinc ions interacts with COF also less when compared to the **HqTp** COF.

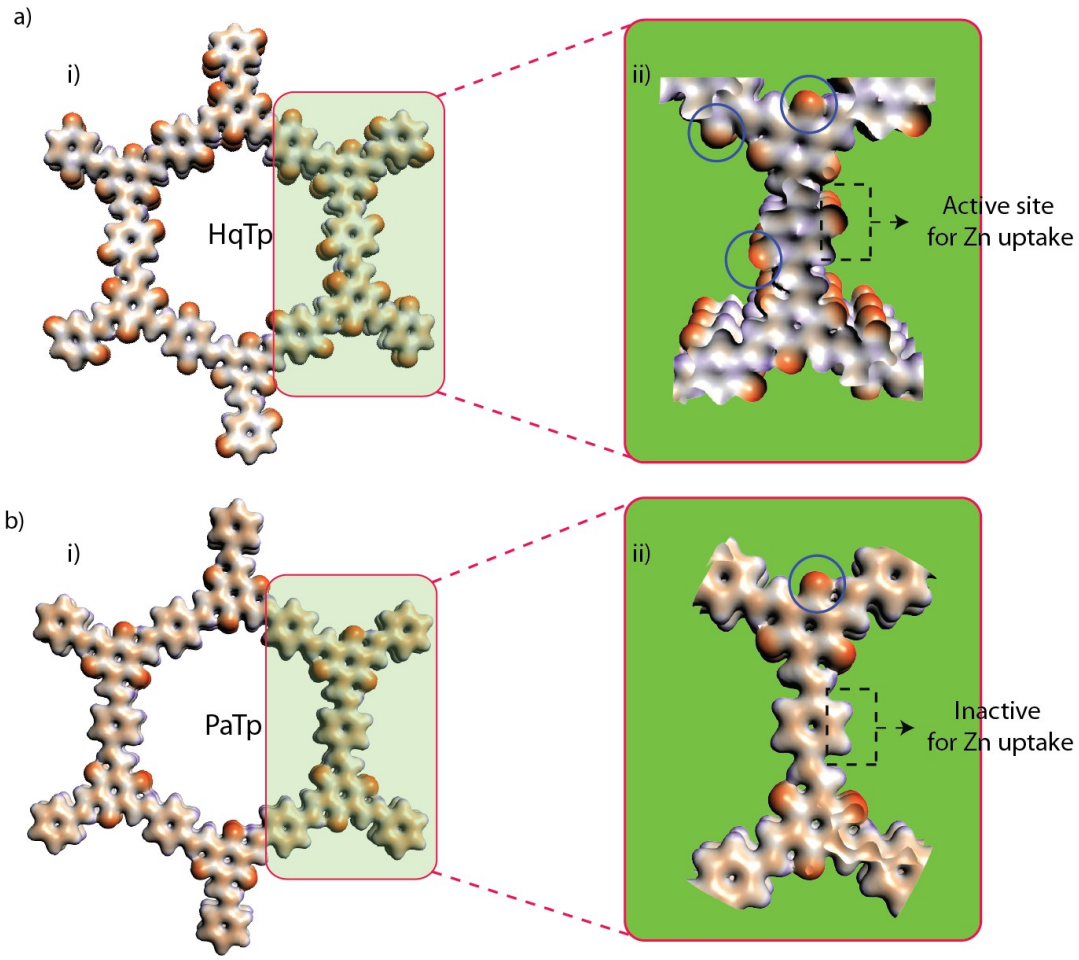

Figure S5: The electro static potential (ESP) mapping of a) **HqTp** and b) **PaTp** COFs by considering a bi-layer single pore and a unit cell. In **HqTp,** the density isosurface (the edge of the "bubble" is 0.03 au and the Coulomb potential ranges from-0.035 au (red) to 0.47 au (blue) for the single pore and -0.33 au (red) to 0.061 au (blue) for the unit cell. Similarly, in **PaTp**, it ranges from -0.054 au (red) to 0.42 au (blue) for the single pore and -0.4 au (red) to 0.066 au (blue) for unit cells. Herein, the negative ESP (red) reflects the affinity of the sites toward the zinc uptake. Therefor, from the ESP calculations, it is clear that quinone C=O, Tp C=O exhibits more –ve compared to the NH sites. Whereas, the ESP of a benzene linked β-ketoenamine **PaTp** COF showcases only Tp C=O groups as active sites for uptaking the Zn^{2+} ions. It further suggests the excellent candidacy of **HqTp** COF.

S-4: FT-IR spectroscopy

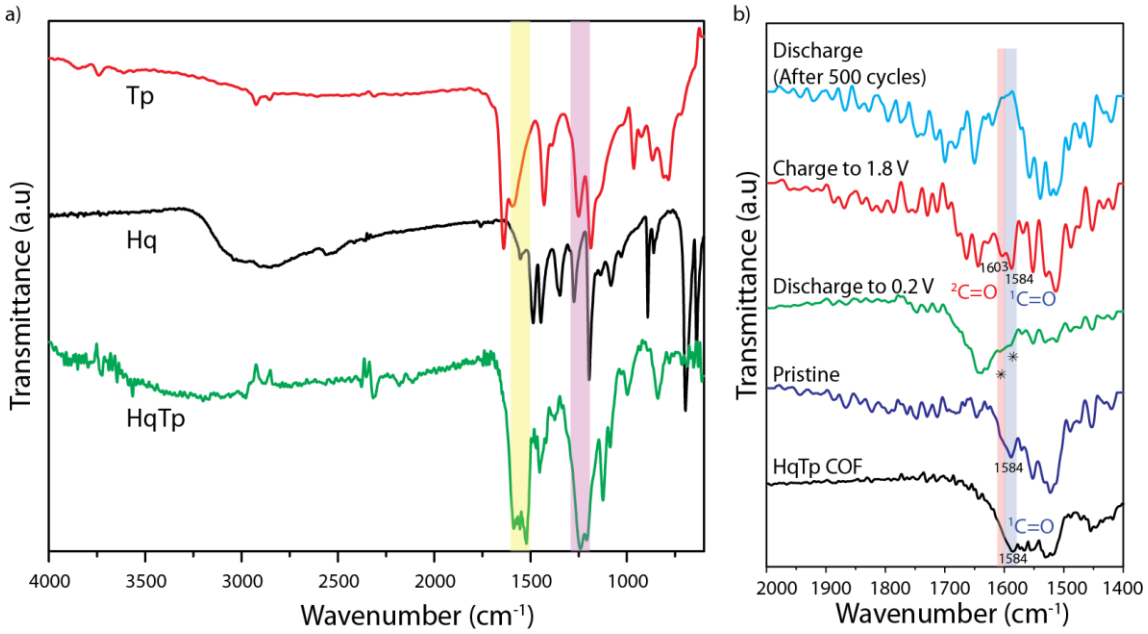

Figure S6: FT-IR spectroscopy of a) **HqTp** and the building units; b) COF after electrochemical analysis

S-5: ^{13}C CP MAS Solid-state NMR

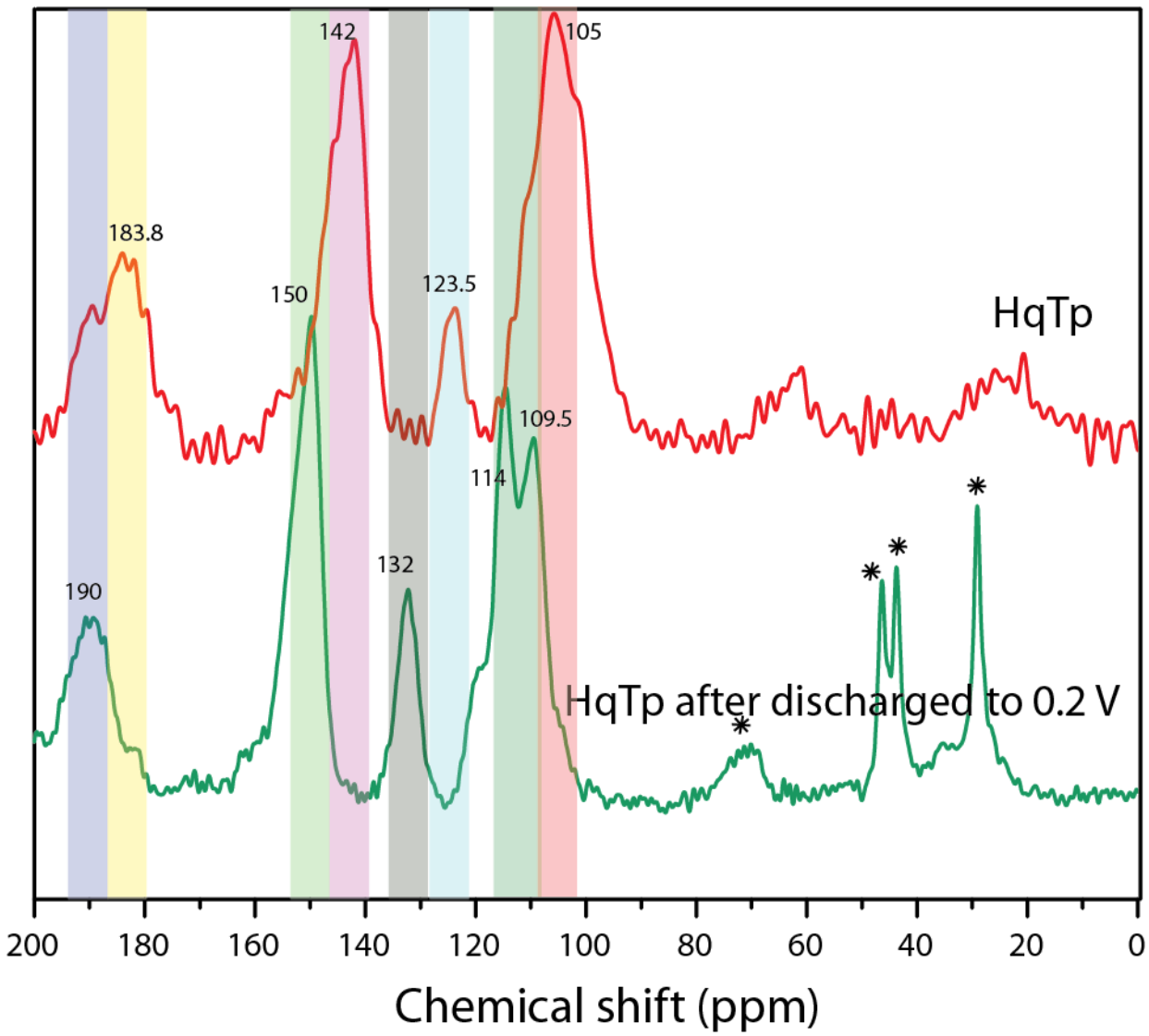

Figure S7: The ^{13}C CP MAS solid-state NMR of pristine **HqTp** COF and after discharged to 0.2 V.

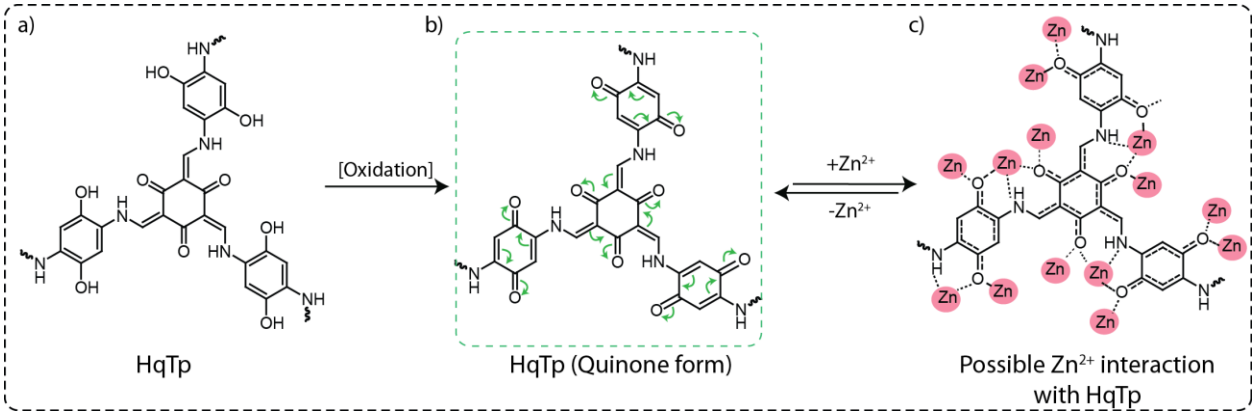

Figure S8: The possible mechanism of the interaction of COF with Zn^{2+} ions during the discharge process in electrochemical reaction.

S-6: TGA & N_2 gas adsorption analysis

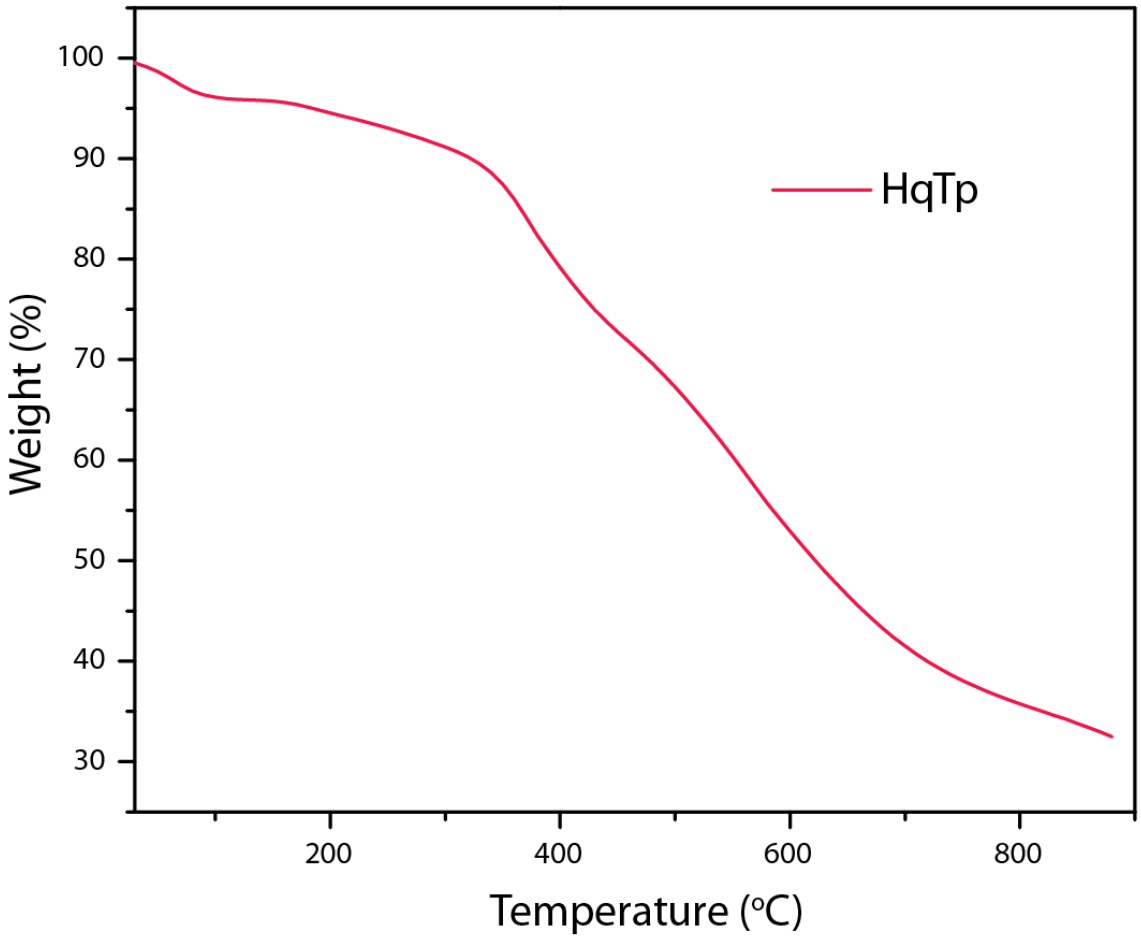

Figure S9: TGA of **HqTp** COF at N_2 atmosphere.

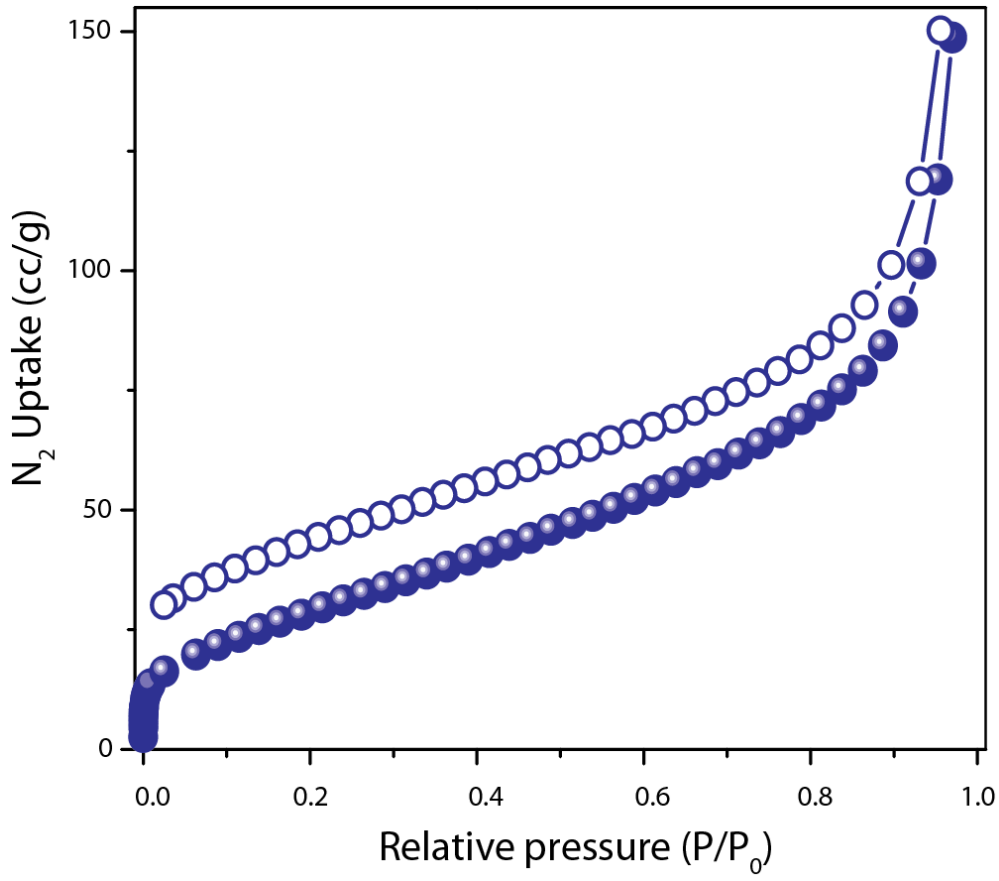

Figure S10: N_2 gas adsorption analysis of **HqTp** COF.

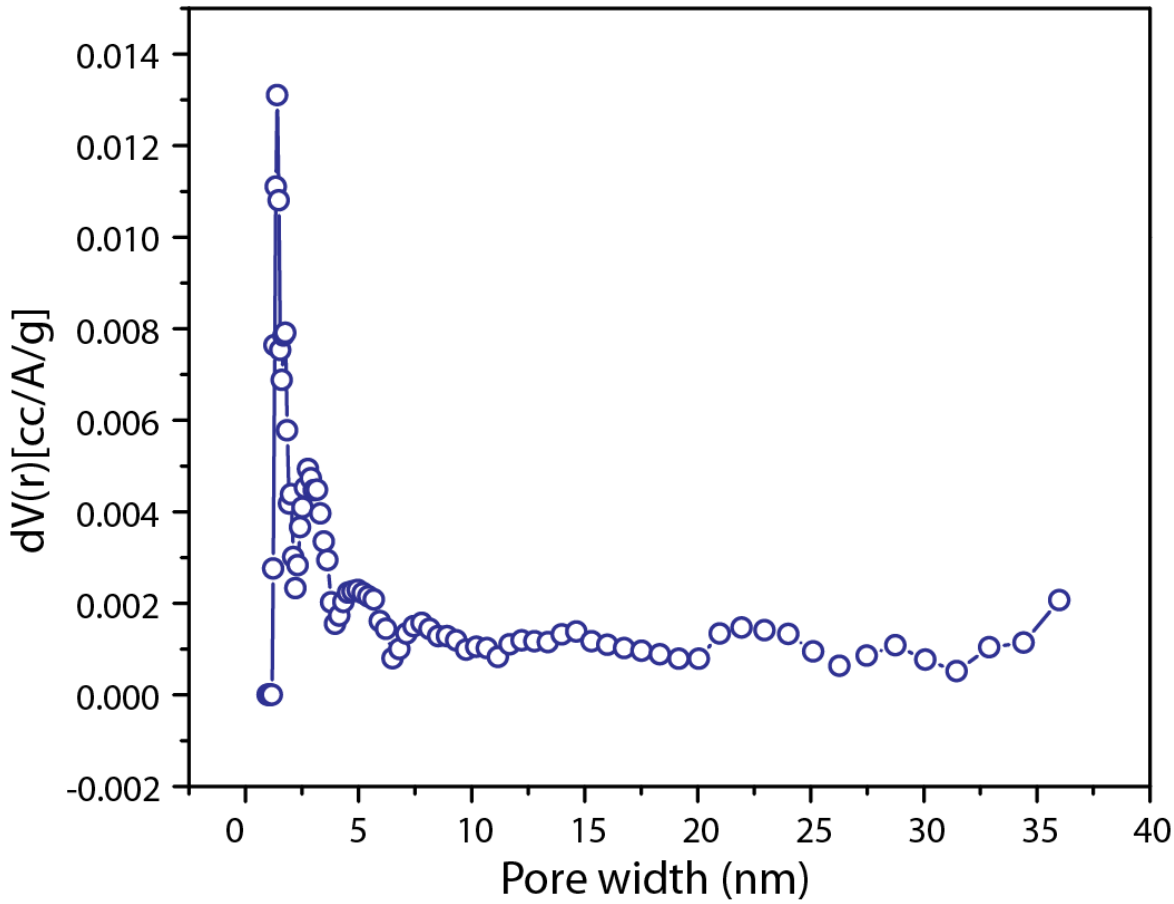

Figure S11: The NLDFT pore size distribution plot of **HqTp** COF.

S-7: TEM and SEM

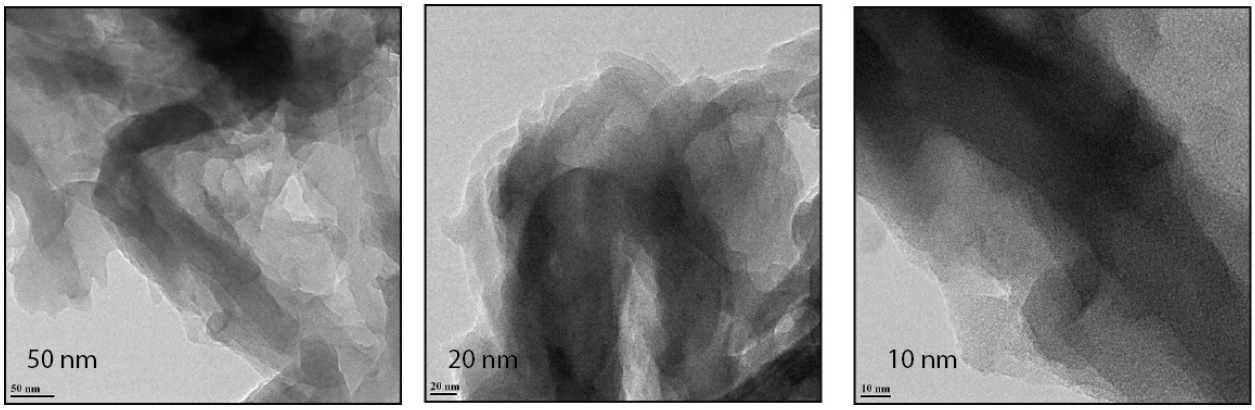

Figure S12: TEM images of **HqTp** COF.

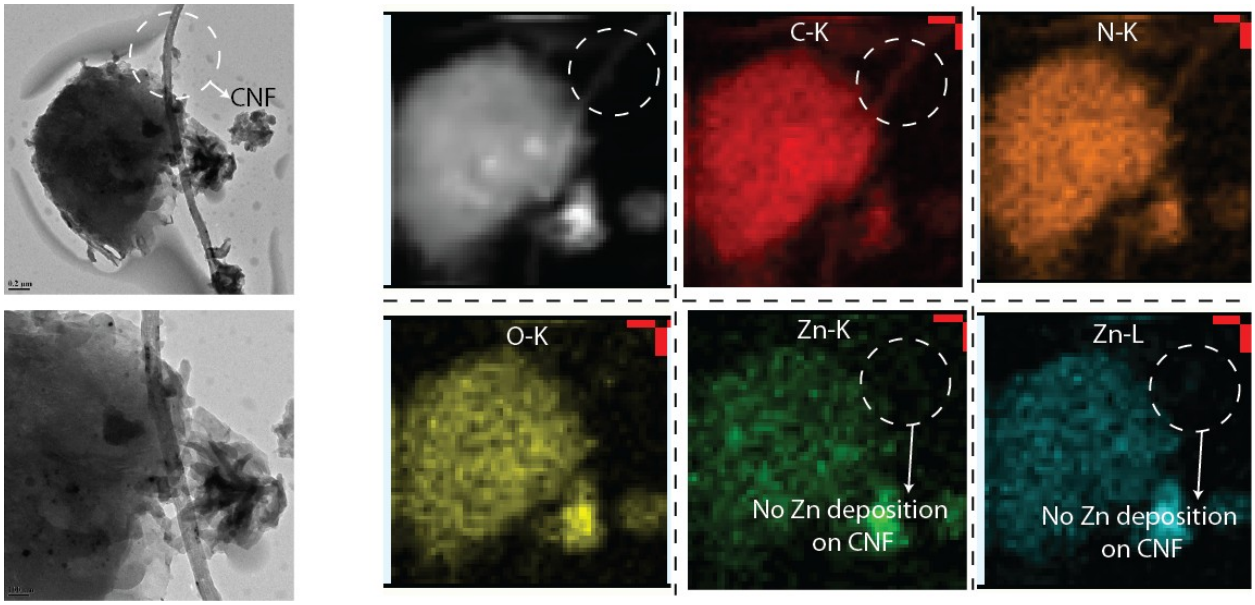

Figure S13: TEM elemental mapping of discharged (0.2 V) cathode of **HqTp** COF.

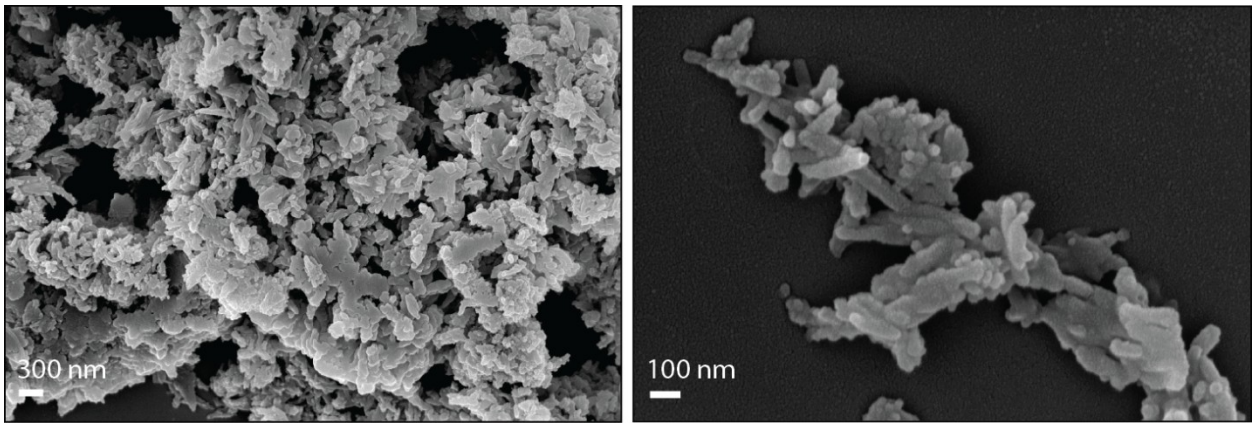

Figure S14: FESEM images of **HqTp** COF.

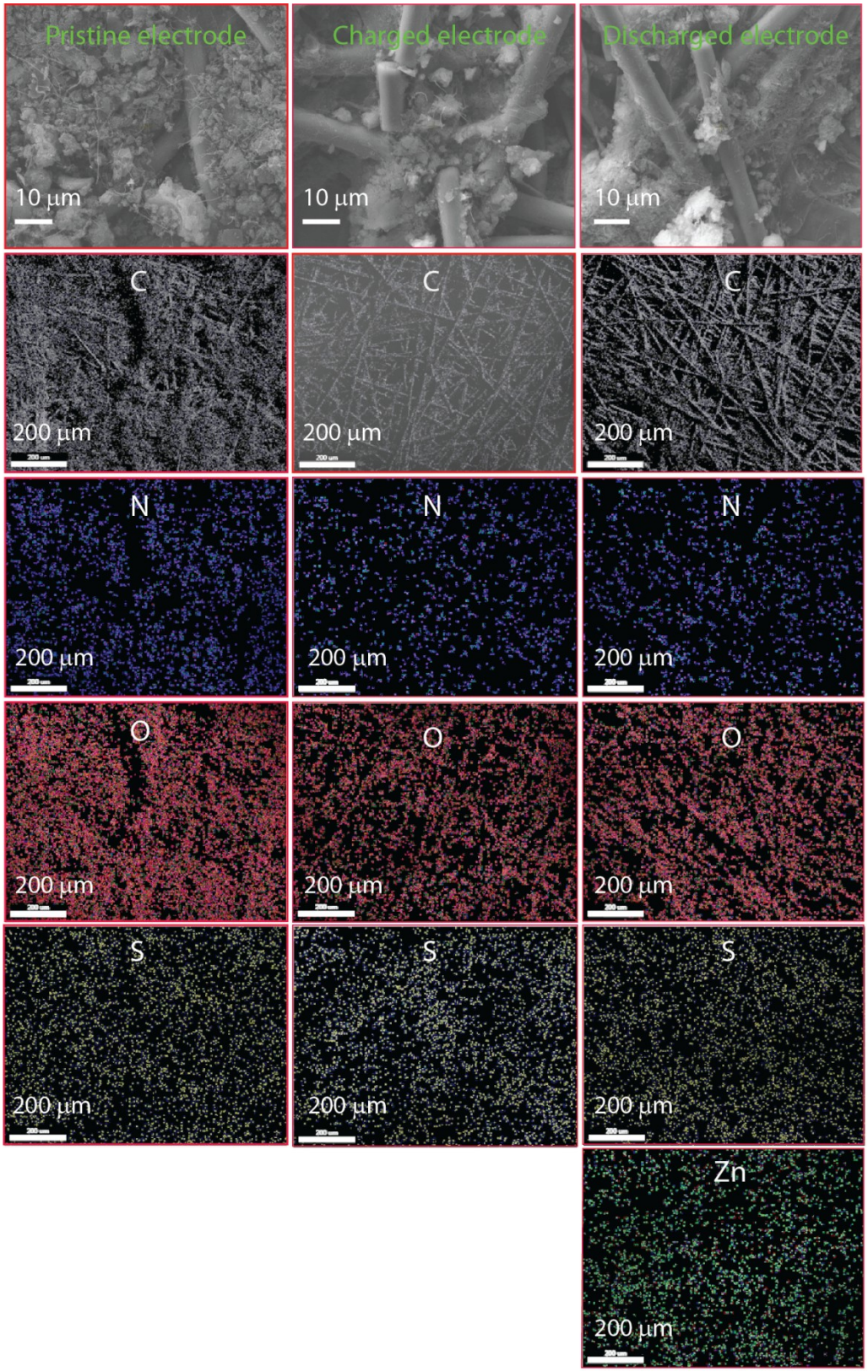

Figure S15: ESEM elemental mapping of pristine, charged (1.8 V) and discharged (0.2 V) cathode of **HqTp** COF.

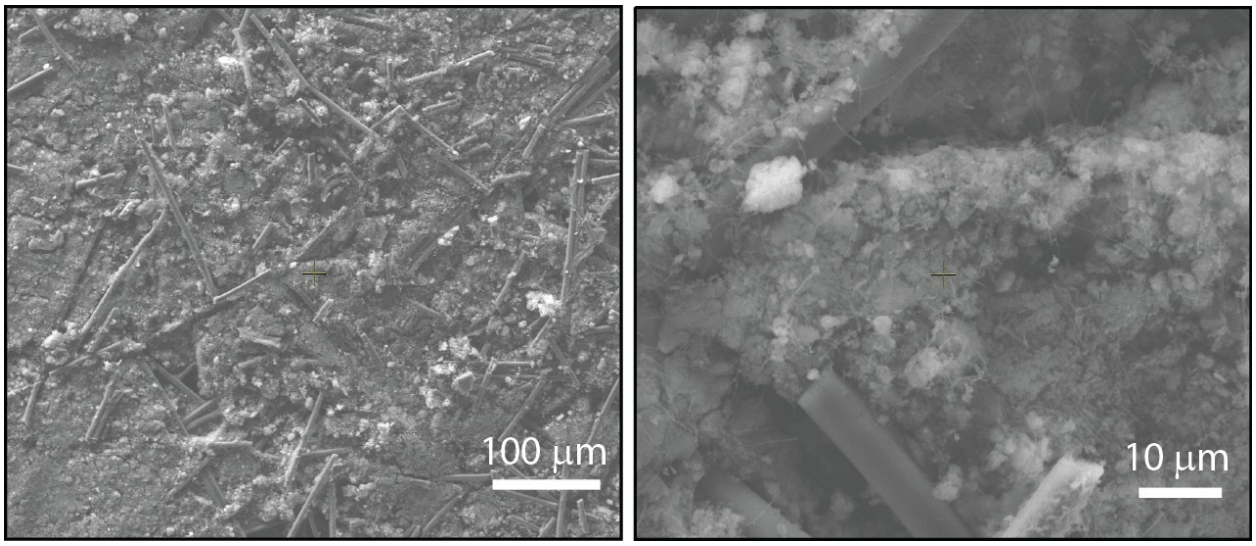

Figure S16: ESEM of **HqTp** cathode after 500 charge-discharge cycles.

S-8: X-ray Photoelectron Spectroscopy

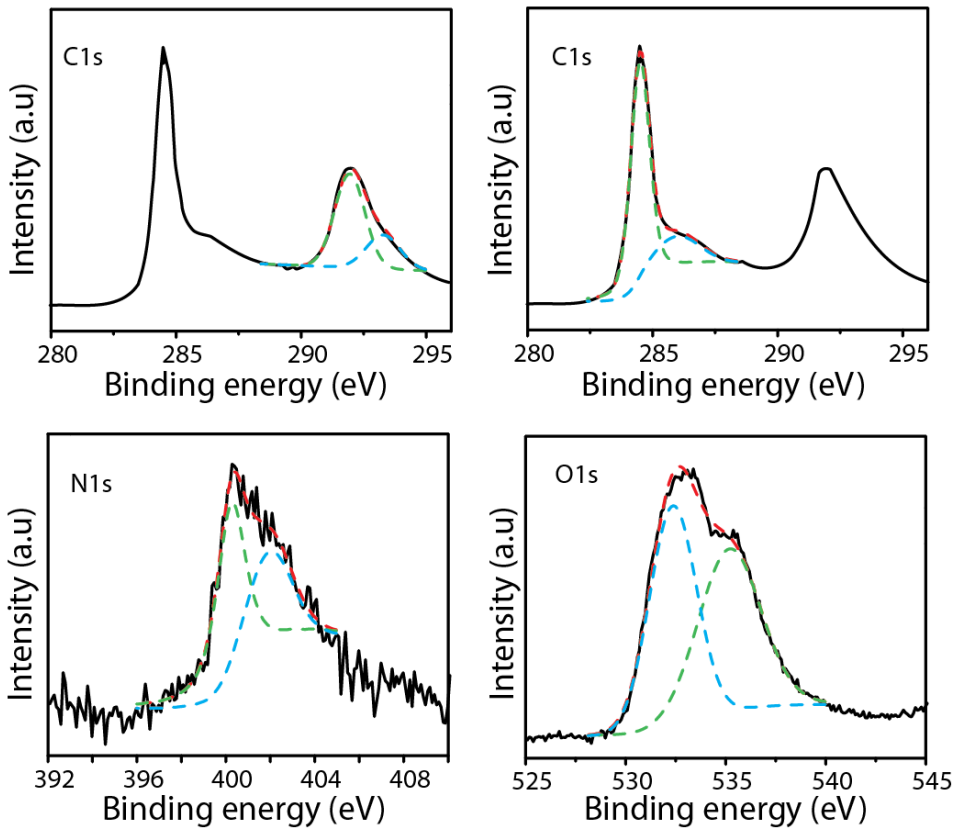

Figure S17: The deconvoluted XPS profiles C1s; N1s & O1s of pristine **HqTp** cathode.

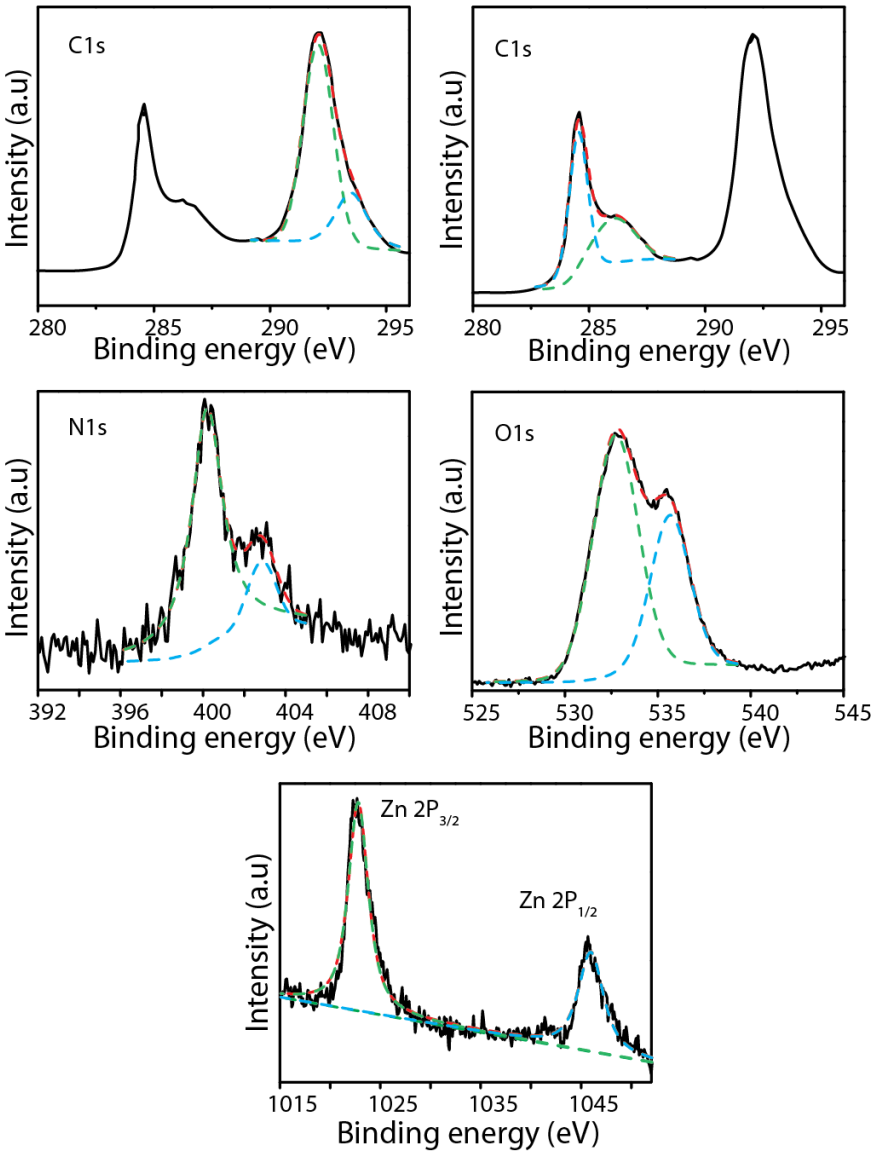

Figure S18: The deconvoluted XPS profiles C1s; N1s & O1s of charged (1.8 V) **HqTp** cathode.

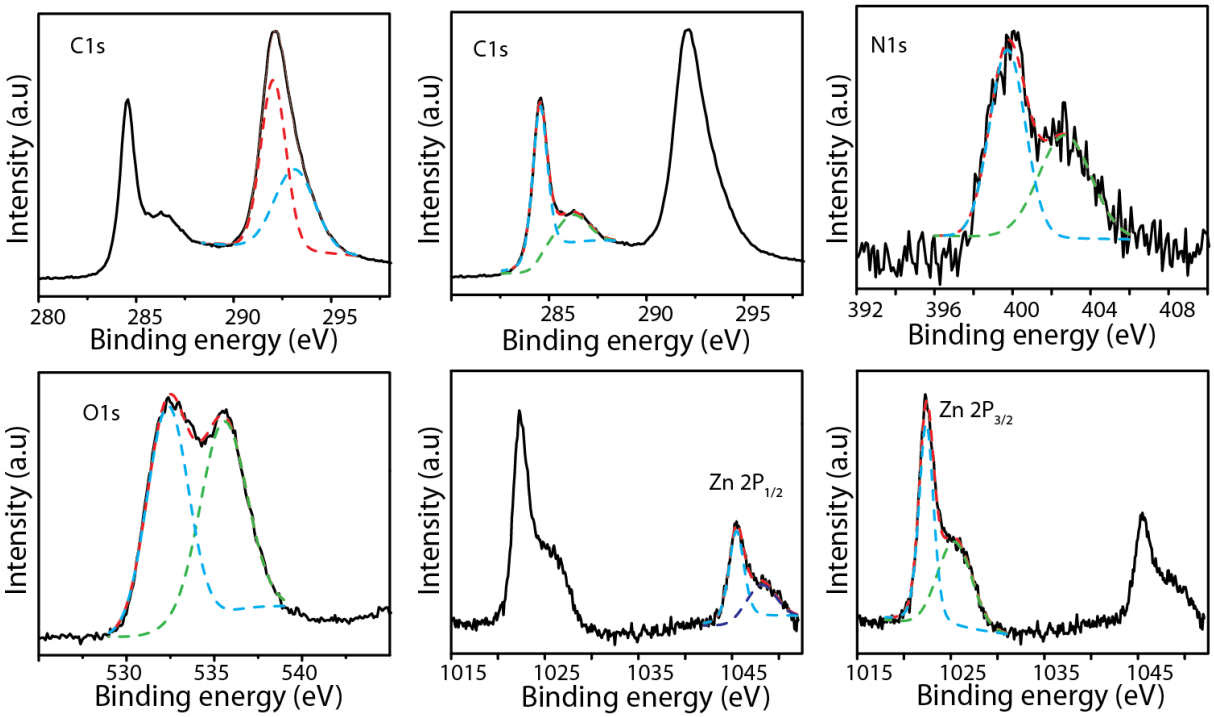

Figure S19: The deconvoluted XPS profiles C1s; N1s & O1s of discharged (0.2 V) **HqTp** cathode.

All XPS samples were analyzed by the direct mounting of the pristine, charged (1.8 V), discharged (0.2 V) electrodes. The charged and discharged electrodes were thoroughly washed with water to remove excess amount of $ZnSO_4$ electrolyte.

S-9: Electrochemical characterization

Fabrication of Zn/HqTp cell- For the fabrication of cathode, uniform slurry was prepared by mixing **HqTp** COF (4 mg) and pristine CNF (1 mg) as conducting additives in 3:1 water-IPA solution (1ml). Later, 5wt% Nafion solution as binder was added into the slurry. The slurry was coated over 1cm^2 area of modified carbon fiber paper to obtain 1 mg cm^{-2} loading of **HqTp** and CNF composite (the hydrophobic surface of pristine carbon fiber paper was modified by anodizing at constant voltage of 10 V for 5 min in 0.1 M Na_2SO_4 solution followed by annealing at 250^{o}C for 2 h to remove the excess surface functional groups). The coated electrodes are dried at 60^{o}C. A piece of metallic Zn foil (1 cm^2 area) was used as an anode. A modified Nafion 212 membrane was applied as separator. The pristine Nafion 212 membrane was treated at 80^o C subsequently with 4wt% H_2O_2, DI water, 0.8M H_2SO_4 and DI water. The pretreated Nafion membrane was stored in aqueous solution of 3M $ZnSO_4$ for two days to ensure complete impregnation of the electrolyte. Finally the cathode, anode and separator were assembled in CR2032 coin cell.

Here, in paper, the terms anode and cathode are used for the negative and positive electrodes, respectively, considering the discharging process of the cell.

Electrochemical characterization- The performance of the **Zn/HqTp** cells was assessed by CV analyses (at scan rates of 1.0, 0.5, and 0.1 mV s^{-1}) and galvanostatic charge/discharge (GCD) (at constant current rates of 125, 312.5, 625, 1250 and 3750 mA g^{-1}) analyses. The cell was operated in a potential range of 1.8V to 0.2 V vs. Zn/Zn^{2+}. The electrochemical impedance spectroscopy was carried out from higher frequency of 1 MHz to lower frequency of 1 Hz against an open circuit potential with a sinus amplitude of 10 mV (V_{rms}= 7.07 mV). The cycling stability of the cell was investigated by GCD experiment at current rate of 3000 mA g^{-1}.

Equations:

1. Specific capacity

The capacity of the **Zn/HqTp** cell is calculated from the galvanostatic charge-discharge plot by using **Equation S1:**

$$\text{Capacity} = \text{Discharge time (hour)} \times \text{applied current density (A } g^{-1}) \times 1000 \quad \text{(Equation S1)}$$

2. Calculation of energy density (ED) and power density (PD)

$$ED = Average \text{ discharge capacity } (mA\ h\ g^{-1}) \times V \quad \text{.... (Equation S2)}$$

where, 'V' is the average voltage (calculation of average voltage is given in Figure S24, Equation S6).

$$PD = \frac{\text{ED}}{\text{Discharge time (hour)}} \quad \text{.... (Equation S3)}$$

3. Calculation of the number discharged of Zn^{2+} ion per unit cell of COF

1. Based on the number of carbonyl groups in the unit cell:

The theoretical specific capacity[4] $= \frac{\text{No.of electrons} \times 96485}{3600 \times \text{Molecular weight}}$ .... (Equation S4) [4]

The number of carbonyl groups in the unit cell (from **Hq** and **Tp**) = 24

If we consider two carbonyls are interacted with one Zn^{2+} ion, maximum number of Zn^{2+} ions interacted in the unit cell of slip AA stacked **HqTp** COF = 24/2 = 12

Total number of electrons = 12 ×2 = 24

Molecular weight of the COF (based on the unit cell) = 1452 $gmol^{-1}$

Therefore, the theoretical specific capacity = $\frac{24 \times 96485}{3600 \times 1452}$ = 0.442 Ahg^{-1} = 442 $mAhg^{-1}$

The experimentally obtained discharge capacity = 276 $mAhg^{-1}$

The efficiency of specific capacity based on the DFTB model = $\frac{\text{Experimental capacity}}{\text{Theoretical capacity}} \times 100$

.... (Equation S5)

= 62.44 %

Therefore the number of discharged Zn^{2+} ion interacted with COF based on the DFTB model = $\frac{62.44 \times 12}{100}$

= 7.49 Zn^{2+} ions per unit cell.

2. Based on the DFTB model of HqTp-Zn:

The theoretical specific capacity = $\frac{\text{No.of electrons} \times 96485}{3600 \times \text{Molecular weight}}$ .... (Equation S4) [4]

Maximum number of Zn^{2+} ions interacted in the unit cell of slip AA stacked **HqTp** COF = 23

Number of electrons from one Zn^{2+} ion = 2

Total number of electrons = 23 ×2 = 46

Molecular weight of the COF (based on the unit cell) = 1452 $gmol^{-1}$

Therefore, the theoretical specific capacity = $\frac{46 \times 96485}{3600 \times 1452}$ = 0.849 Ahg^{-1} = 849 $mAhg^{-1}$

The experimentally obtained discharge capacity = 276 $mAhg^{-1}$

The efficiency of specific capacity based on the DFTB model = $\frac{\text{Experimental capacity}}{\text{Theoretical capacity}} \times 100$ …. (Equation S5)

= 32.5 %

Therefore the number of discharged Zn^{2+} ion interacted with COF based on the DFTB model = $\frac{32.5 \times 23}{100}$

= 7.47 Zn^{2+} ions per unit cell.

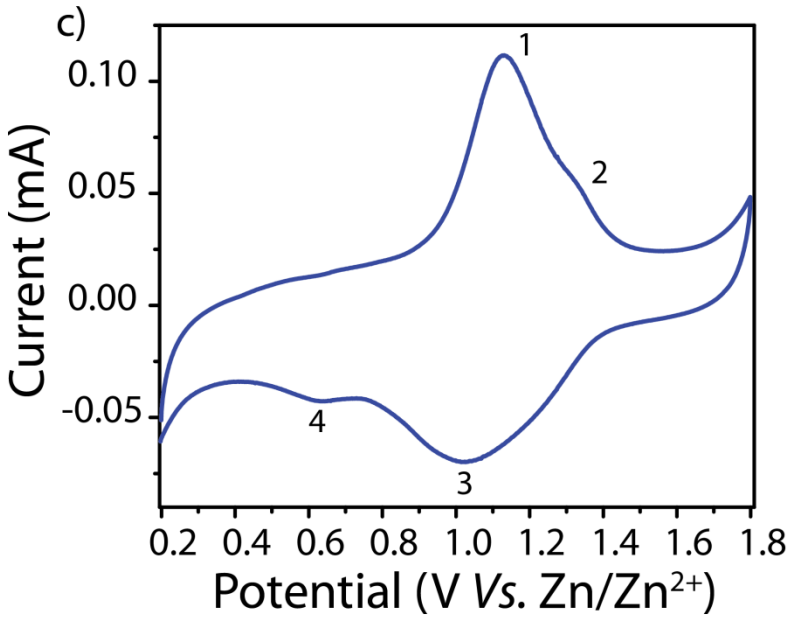

Figure S20: CV of **HqTp** COF at 0.1 $mVsec^{-1}$.

The CV profile of the **HqTp** COF exhibits a set of redox peaks with onset potentials (The potential where the peak is started to form) is situated at 0.9 V (peak 1) and 1.4 V (peak 3) vs. Zn/Zn^{2+} (Figure S20). As it can be observed in the same CV, two additional weak peaks (the onset potentials of oxidation peak and reduction peaks are at 1.30 (peak 2) and 0.73 V (peak 4) vs. Zn/Zn^{2+}, respectively) are also observed. The peaks 1 and 2 are easily distinguishable but at the same time the redox pair of peak 2 is not visible in the reduction half. However, considering the broadness of the peak 3, it can be concluded that the redox pair of peak 2 is in fact merged

within the peak 3 (*R. Gulaboski, P. Kokoškarova and S. Mitrev, Electrochim. Acta, 2012, 69, 86–96*). It is worth mentioning that the peak 4 is not reversible but it is present only at a low scan rate as low as 0.1 mV sec^{-1}. However, if the higher scan rates, for instance 0.5 and 1 mV sec^{-1} are considered (Figure S21), the peak (2) and (4) are not apparent. Moreover, the current response obtained from the peak 2 and 4 even at 0.1 mV sec^{-1} are negligible and do not contribute much to the capacity. Hence it can be concluded that the peaks 1 and 3 are the signature peaks corresponding to the reversible shuttling of the Zn^{2+}-ions.

Notably, only the Tp C=Os are responsible for the redox activity in the **PaTp** COF. A pair of weak redox peaks is present in the CV profile of **PaTp** at 1 mV sec^{-1} (Figure S23). Taking this into account, we assume, the weak peak 2 in the CV of **HqTp** could be originated from the Tp C=O and the corresponding reduction peak could be merged with peak 3.

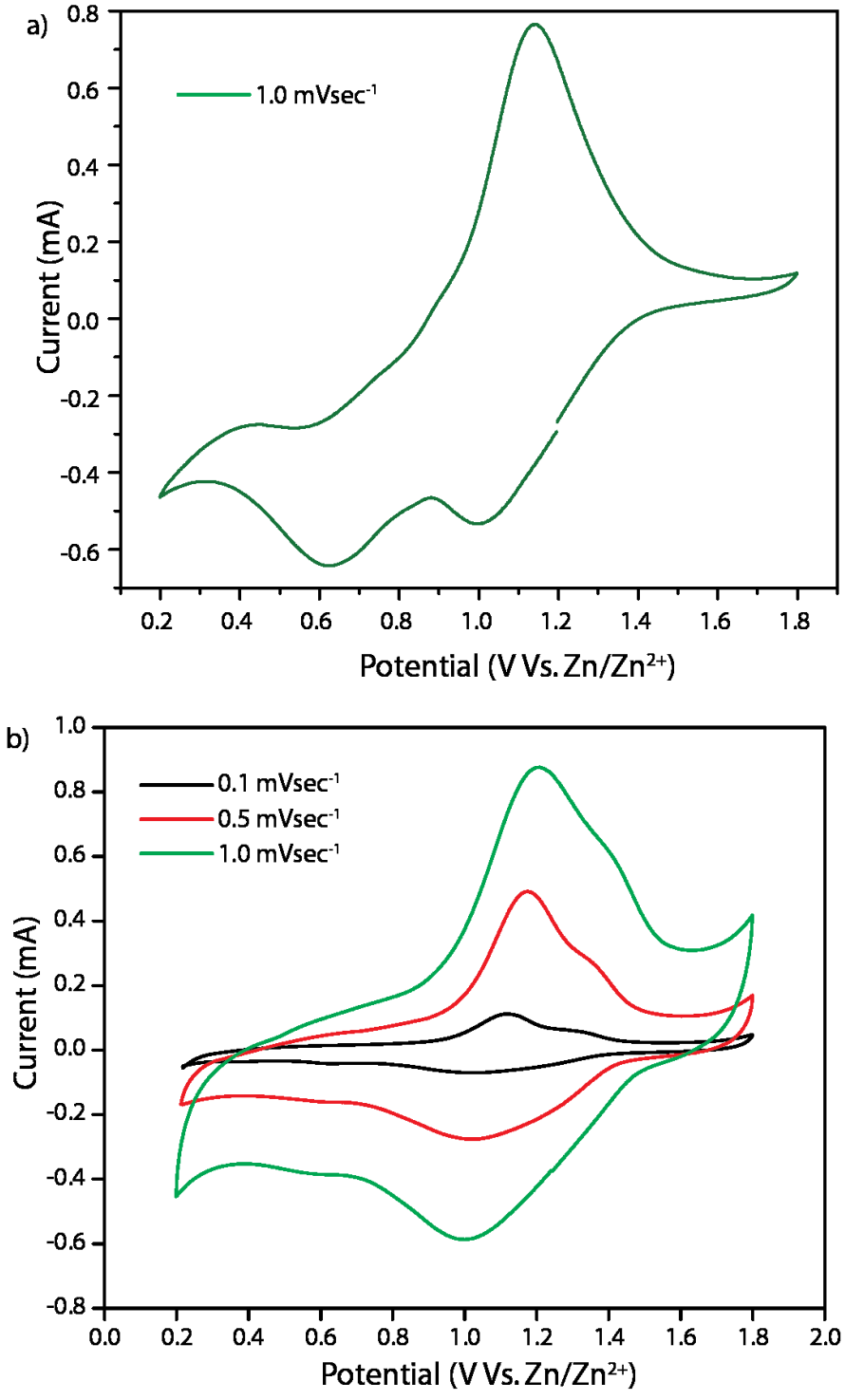

Figure S21: a) Cyclic voltammetry of **HqTp** COF in three electrode experiment at the scan rate of 1 $mVSec^{-1}$ b) Cyclic voltammetry of **HqTp** COF in two electrode device experiment at different scan rates.

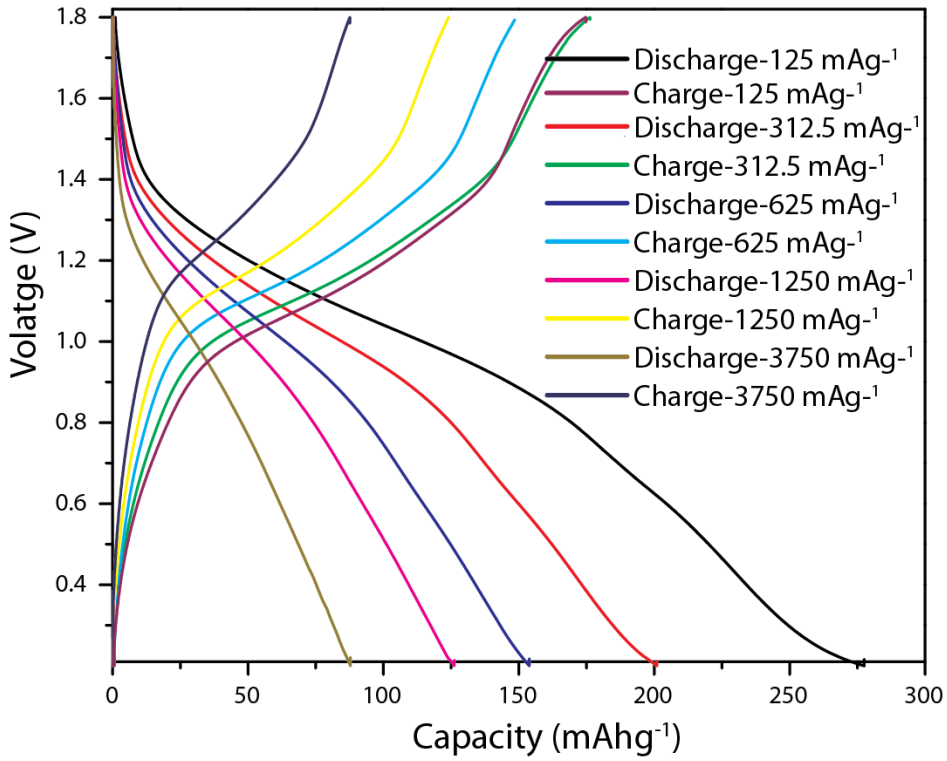

Figure S22: Galvanostatic charge-discharge analysis of **HqTp** COF at different scan rates.

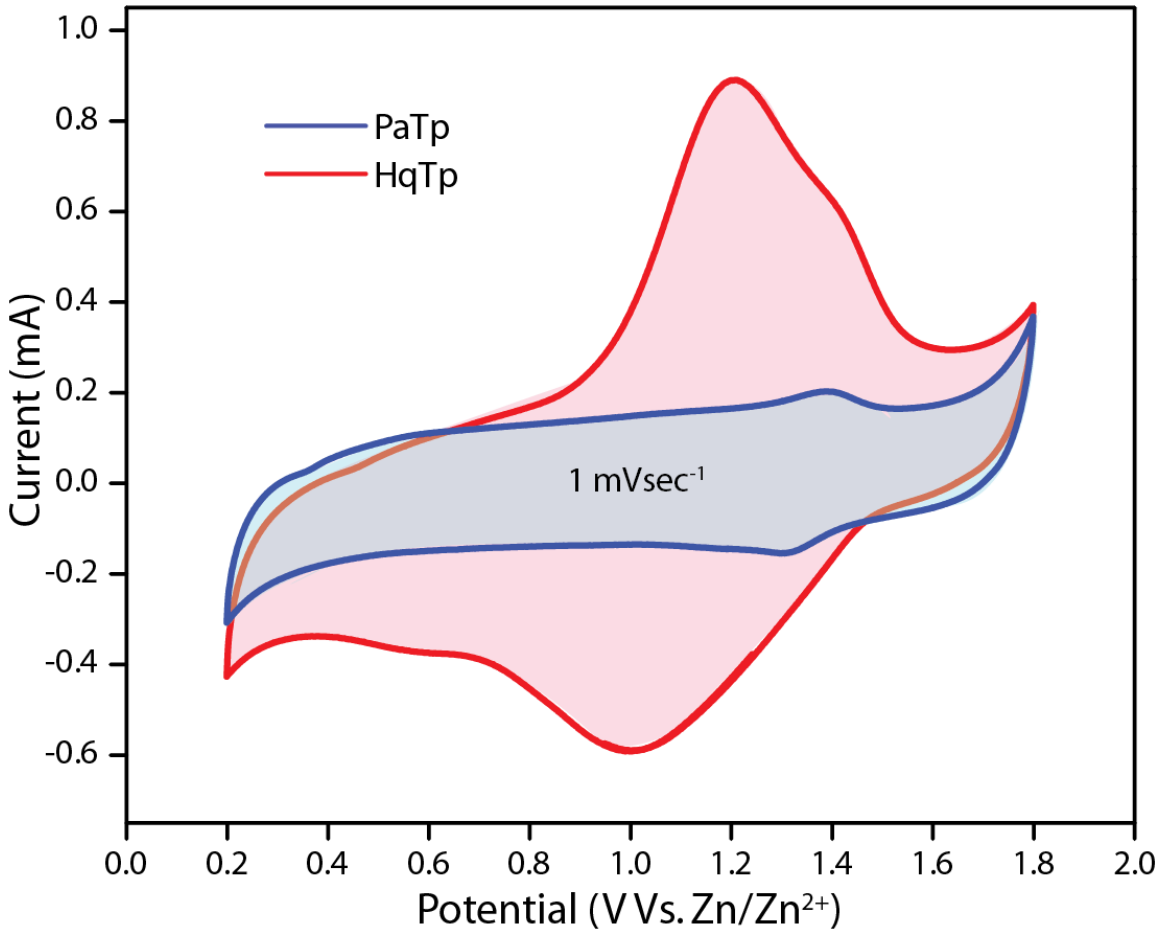

Figure S23: Comparison of CV profile of **HqTp** and **PaTp** at the scan rate of 1 $mVsec^{-1}$.

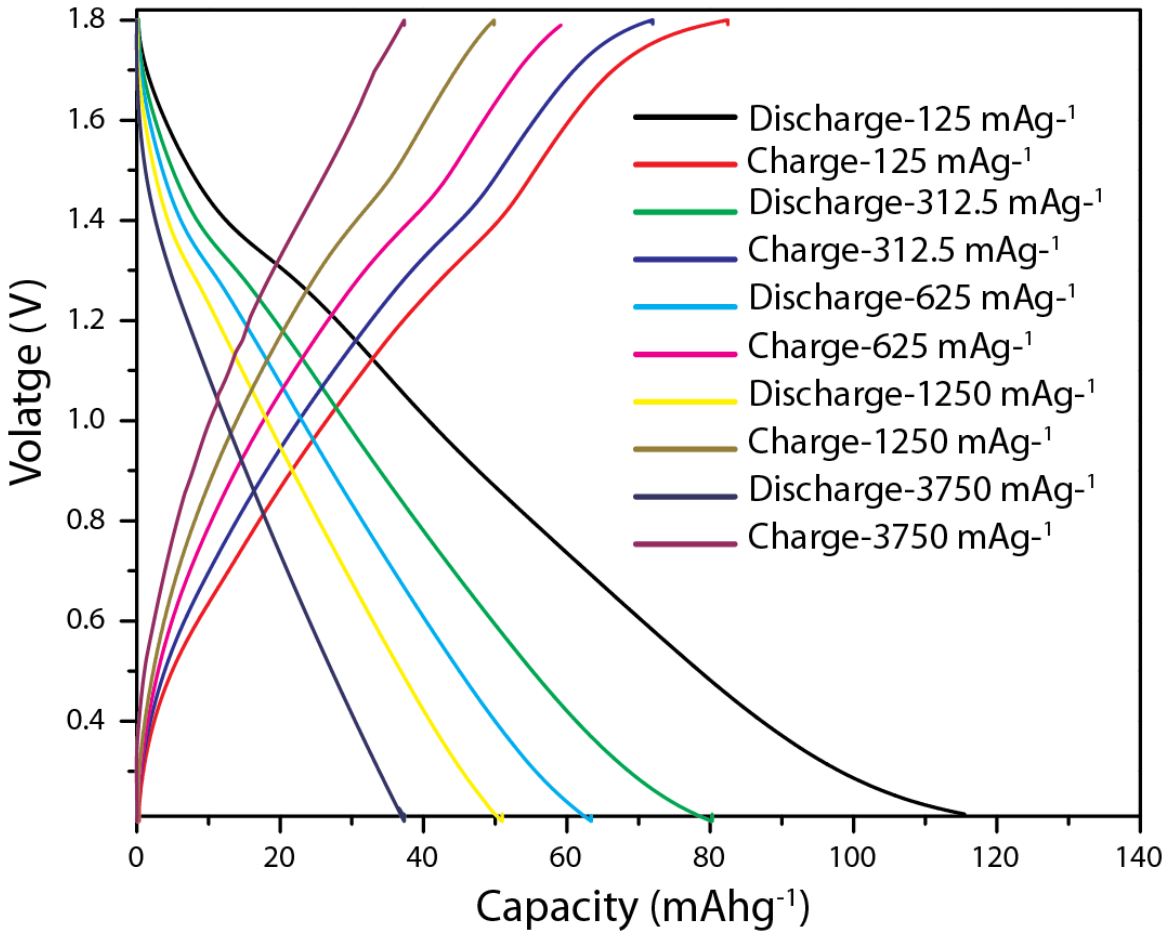

Figure S24: Galvanostatic charge-discharge analysis of **PaTp** COF at different scan rates.

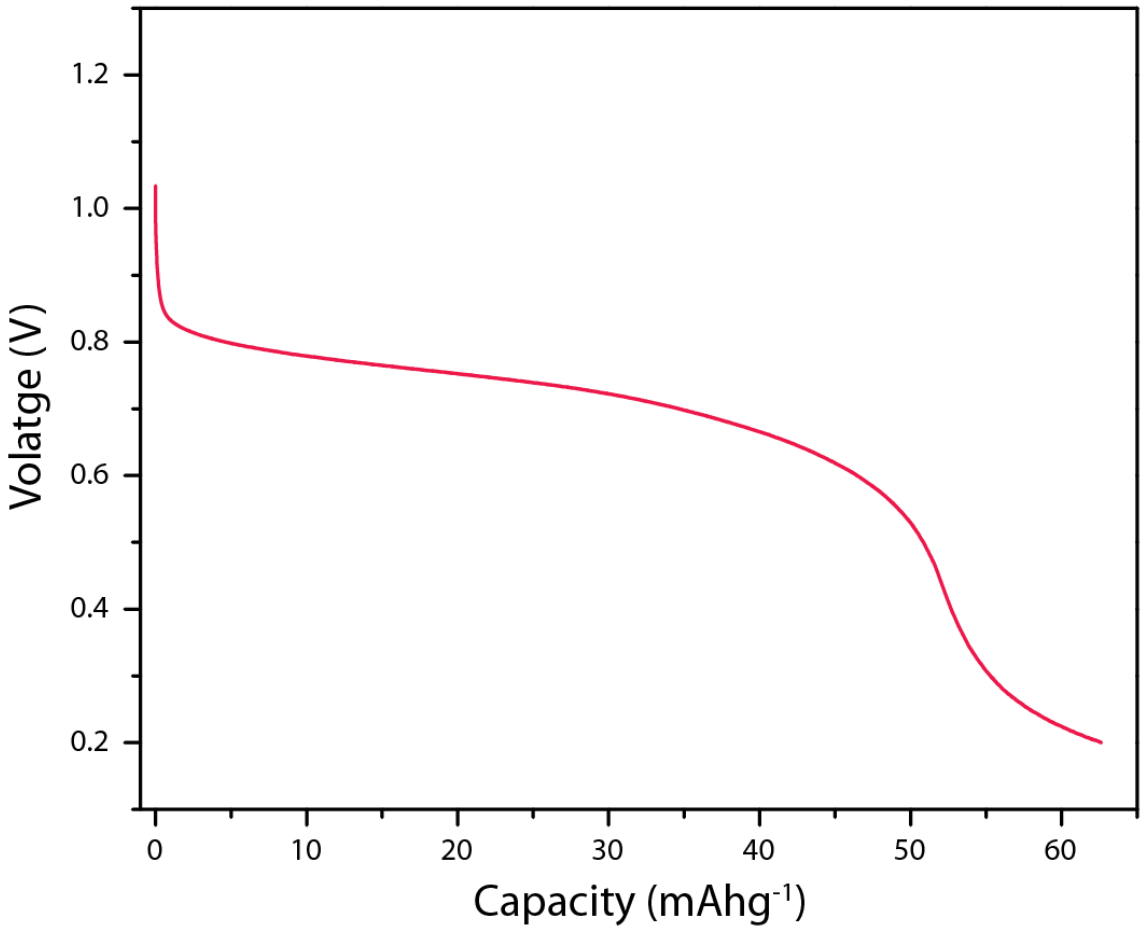

Figure S25: The galvanostatic discharging experiment (conducted at OCV) of **HqTp** COF at very high loading (60 mg).

The electrochemical analysis of 60 mg of active material on the electrode has been investigated for checking the efficiency of the high loading performance.

For the fabrication of cathode, the uniform slurry was prepared by mixing **HqTp** COF (60 mg) and pristine CNF (15 mg) as conducting additives in 3:1 water-IPA solution (12 ml). Later, 5wt% Nafion solution as binder was added into the slurry. The slurry was coated over 4 cm^2 area of modified carbon fiber paper to obtain 15 mg cm^{-2} loading of **HqTp** and CNF composite. The coated electrodes are dried at 60^oC. A piece of metallic Zn foil with thickness of x um (4 cm^2 area) was used as an anode. Herein, we dipped both electrodes in 3M $ZnSO_4$ electrolyte and the then the discharge analysis has been done.

The galvanostatic discharging experiment of **HqTp** COF at very high loading at the current rate of 16 mAg^{-1} delivered a specific capacitance of 66 $mAhg^{-1}$. Similarly, the areal capacitance is

noted 0.97 $mAhcm^{-2}$ at the current rate 0.25 $mAcm^{-2}$. The discharged COF is taken for the further analysis of ^{13}C CP MAS solid-state NMR.

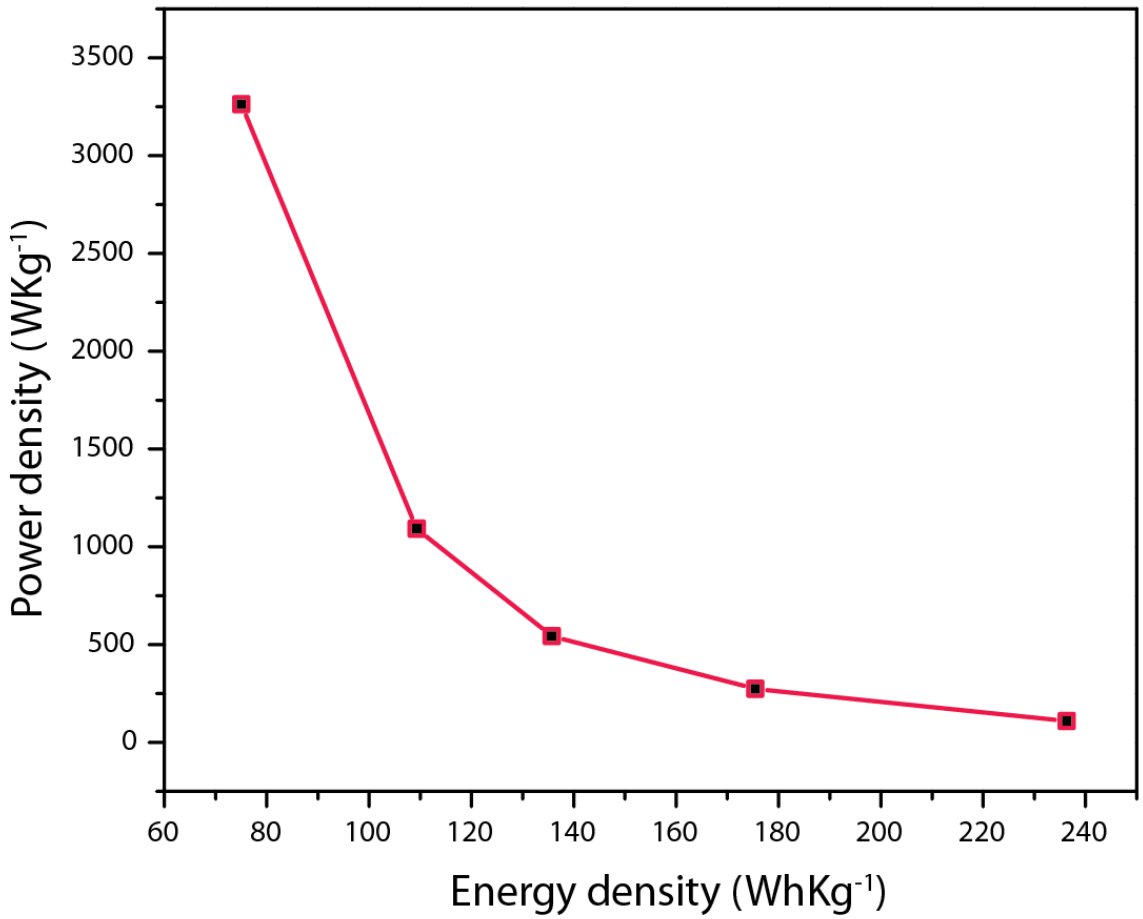

Figure S26: Ragone plot of **HqTp** COF.

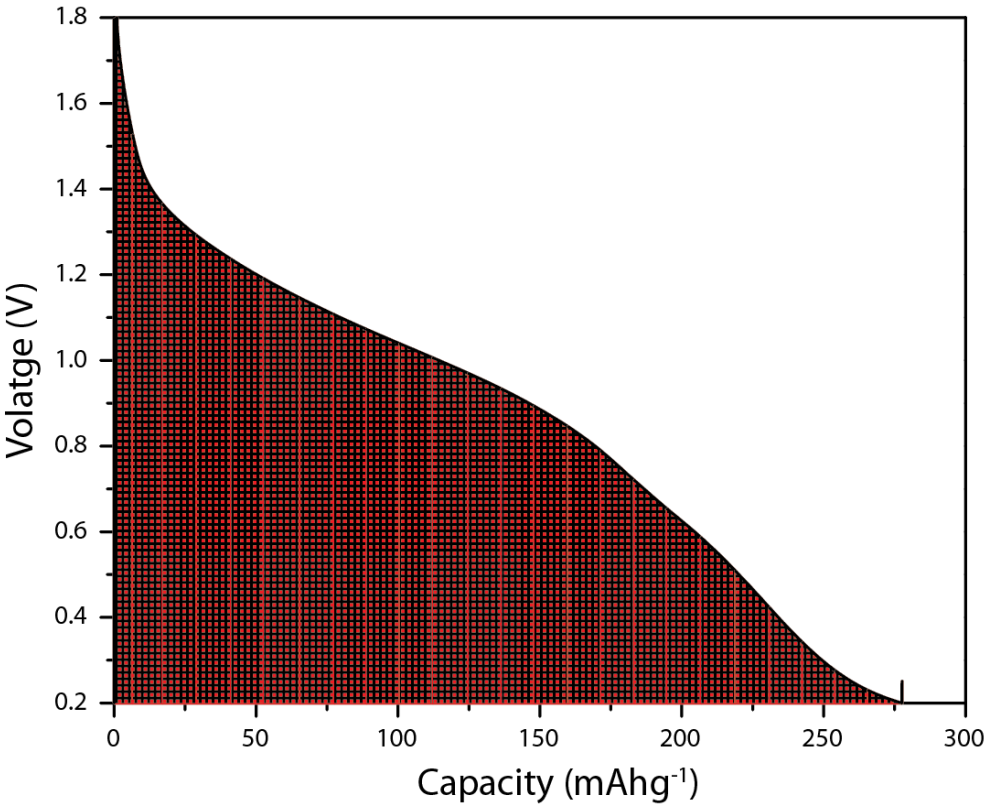

Figure S27: Voltage *vs.* discharge capacity plot of **HqTp** COF at a current rate of 100 mA g^{-1}

The average voltage was calculated by integrating the area under the voltage *vs.* discharge capacity plot at a current rate of 0.10 A g^{-1}. The area indicated in the above plot equals to the specific energy density based on the loading of active material on cathode.[5] The integrated area from Figure S27 is calculated to be 240 Whkg^{-1} and the corresponding discharge capacity is 276 mA h g^{-1}. Therefore, the average voltage can be calculated from the following equation.

$$\text{Average voltage} = \frac{Specific\ energy\ density}{Discharge\ capacity} = \frac{240}{276} = 0.87\ \text{V} \quad \text{..... (Equation S6)}$$

This average voltage value is used in Equation S2 for calculating energy density at other current rates.

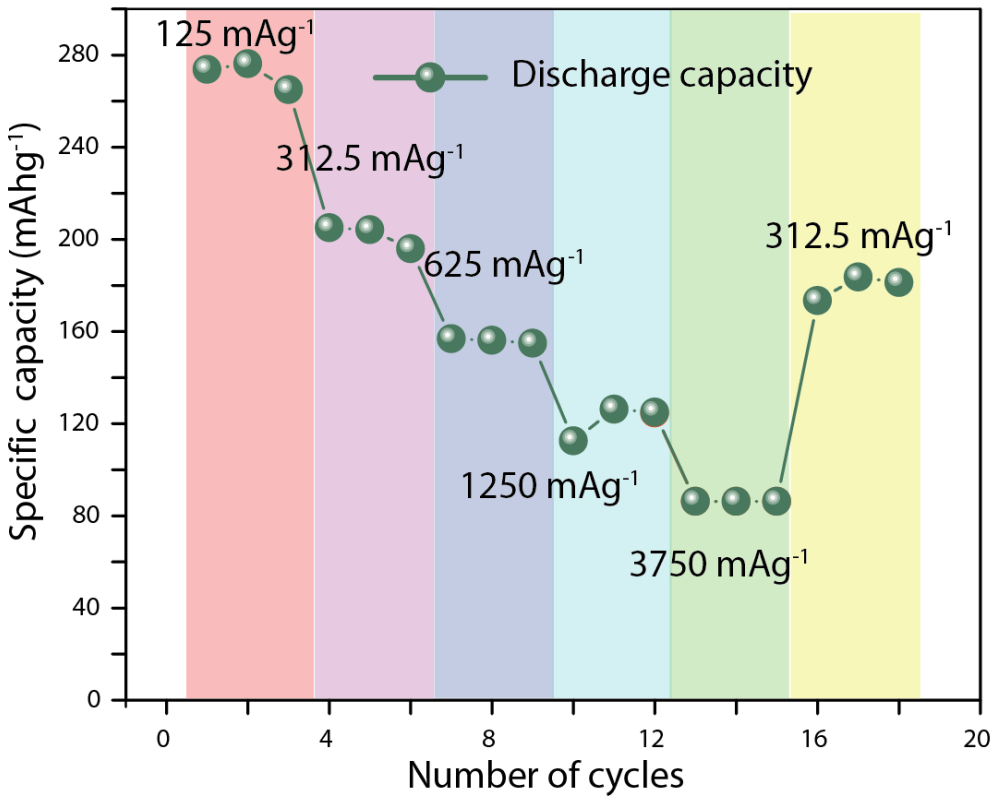

Figure S28: Rate performance of **HqTp-ZIB.**

The features of charge-discharge curves of HqTp COF in ZIB:

The **HqTp** organic cathode is operable at the potential window of 0.2 to 1.8 V *vs*. Zn/Zn^{2+} and provides a high discharge capacity of 276 $mAhg^{-1}$ with excellent cycling stability (95% retention of capacitance after 1000 continuous charge-discharge cycles). The material shows charge-storage behavior throughout the voltage window mentioned above, which is clear from both the galvanostatic charge-discharge as well as from the CV profiles (Figure 4 in the main text and Figure S21 & S22 in the ESI). The selection of an optimized potential window largely depends on the material properties. Although some of the metal-based zinc ion batteries are reported in the potential window of 1-2 V, most of the organic cathodes of zinc ion batteries have been reported in the literature ranging from 0.2 to 1.8 V. Notably, it shows appreciable charge storage in this range of potential window.

The absence of voltage plateau in zinc ion batteries:

We have observed the absence voltage plateau in charge-discharge curves of **HqTp** organic cathode. Meanwhile, the voltage plateau in the charge-discharge profile is absent in some cases of metal based ZIB also. Moreover, many cathode materials have been explored for zinc-ion

batteries have different sets of voltage window and shows charge-storage properties despite the absence of voltage plateau. It has been observed that MnO_2 depending on their crystal structure could display charge-storage properties despite the absence of voltage plateau (Table S1, column 1). Similarly, another popular cathode material for zinc-ion battery, *viz*., V_2O_5 (Vanadium based cathodes), also displays good charge-storage behavior but do not exhibit a well-defined sharp voltage plateau (Table S1, column 2).

Reference for the absence of voltage plateau for Mn based cathodes	**Reference for the absence of voltage plateau for V based cathodes**
H. Pan et al., Nat. Energy, 2016, 1, 16039	*C. Xia et al., Angew. Chem. Int. Ed. 2018, 57, 1 – 7*
D. Kundu et al., Nat. Energy, 2016 1, 16119	*D. Chao et al., Adv. Mater. 2018, 1803181*
C. Xu et al., Angew. Chem. Int. Ed. 2012, 51, 933 –935	*V. Soundharrajan et al., Nano Lett., 2018, 18, 4, 2402-2410*
Y. Jin et al., Adv. Mater. 2019, 1900567	*F. Wan et al., Nat. Commun., 2018, 9 , 1656*
N. Zhang et al., J. Am. Chem. Soc. 2016, 138, 12894−12901	*J. Ding et al., Adv. Mater. 2018, 30, 1800762*
Y. Li et al., Chem. Mater. 2019, 31, 2036−2047	*N. Zhang et al., ACS Energy Lett. 2018, 3, 1366−1372*
S.-D. Han et al., Chem. Mater. 2017, 29, 4874−4884	*Y. Yang et al., Energy Environ. Sci., 2018,11, 3157-3162*
L. Wang et al., ACS Sustainable Chem. Eng. 2018, 6, 16055−16063	*P. He et al., Small 2017, 13, 1702551*
J. Wang et al., J. Mater. Chem. A, 2019, 7, 13727–13735	*P. Hu et al., ACS Appl. Mater. Interfaces 2017, 9, 42717−42722*

Table S1: References for the absence of voltage plateau in metal (MnO_2 and V_2O_5) cathode based zinc ion batteries.

It is important to note that, in the case of zinc-ion batteries, capacitive-like charge-discharge profiles (charge-discharge profiles without voltage-plateaus are known as *capacitive-like charge-discharge profiles*) are very common in the literature. Therefore, zinc-ion batteries are called as zinc-ion hybrid capacitors/ battery as well (Table S2). A hybrid capacitor can deliver high energy density and power density concurrently in a particular potential range. In this aspect, the hybrid capacitors are well accounted in those devices which require high energy and power density at a time for an operating potential window.

Active material (Cathode)	**Reference**
Porous Framework Zinc Pyrovanadate	*C. Xia et al., Adv. Mater. 2018, 30, 1705580*
Co-polymer derived hollow carbon spheres (HCSs)	*S. Chen et al., J. Mater. Chem. A, 2019, 7, 7784–7790*
Porous V_2O_5	*P. Hu et al., ACS Appl. Mater. Interfaces 2017, 9, 42717−42722*
Activated carbon	*P. Zhang et al., Adv.Mater.2019, 31, 1806005*
Review on 'metal ion hybrid capacitors'	*L. Dong et al., J. Mater. Chem. A, 2019, 7, 13810–13832*

Table S2: References for hybrid capacitive zinc ion batteries.

Notably, for COF based materials in lithium or sodium-ion batteries, it is very common that the charge discharge-profiles are without voltage plateaus and exhibit hybrid capacitive-like charge-discharge curves (Table S3, Figure 1). This made us believe that voltage plateau may not necessarily important for a material to exhibit the candidacy towards the potential applications.

COFs	Reference
DAAQ-ECOF	*S. Wang et al., J. Am. Chem. Soc. 2017, 139, 12, 4258-4261*
DAAQ-COF	S. Gu et al., *doi.org/10.1021/jacs.9b03467*
PIBN-G COF	*Z. Lou et al., Angew. Chem. Int. Ed. 2018, 57, 9443 –9446*

Table S3: References for the COFs exhibits charge-discharge curves without a voltage plateau in lithium and sodium ion batteries.

Cathode material	Electrolyte	Voltage (Voltage window) [V]	Specific capacity [$mAhg^{-1}$]	Retention(%/ no. of cycle)	Reference
HqTp COF	**3M $ZnSO_4$**	**0.2–1.8 (1.6)**	**276 (100 $mAhg^{-1}$)**	**95/1000 (3.75 Ag^{-1})**	**This work**
α-MnO_2	1 M $ZnSO_4$ or 1 M $Zn(NO_3)_2$	1–1.9 (0.9)	210 (0.5C)	77/100 (6C)	6
V-doped	1 M $ZnSO_4$	1–1.8 (0.8)	266 (66 mA g^{-1})	49/100 (66 mAg^{-1})	7
α-MnO_2 nanorod	α-MnO_2 nanorod 1 M $ZnSO_4$	1–1.8 (0.8)	233 (83 mA g^{-1})	65/50 (83 mA g^{-1})	8
Todorokite [3 × 3]	1 M $ZnSO_4$	0.7–2 (1.3)	108 (0.5C)	95/50 (0.2C)	9
α-MnO_2/CNT	2 M $ZnSO_4$ + 0.5 M $MnSO_4$	1–1.9 (0.9)	190 (100 mA g^{-1})	100/300 (1 A g^{-1})	10
Polypyrrole coated α-MnO_2	Gelatin + Borax polymer aqueous	0.8–1.8 (1)	143.2 (1C)	94/500 (2C)	11
R-MnO_2	1 M $ZnSO_4$ + 0.05 M $MnSO_4$	1–1.8 (0.8)	220 (60 mA g^{-1})	95/100 (60 mA g^{-1})	12
δ-MnO_2	0.5 M AN $Zn(TFSI)_2$	0.05–1.9 (1.85)	123 (12.3 mA g^{-1})	60/100 (0.04C)	13
λ-MnO_2/C	3 M $Zn(CF_3SO_3)_2$	0.8–2 (1.2)	150 (500 mA g^{-1})	94/500 (500 mA g^{-1})	14
Mn_2O_3	2 M $ZnSO_4$	1–1.9 (0.9)	148 (100 mA g^{-1})	87/2000 (100 mA g^{-1})	15
Mn_3O_4	2 M $ZnSO_4$	0.8–1.9 (1.1)	239.2 (100 mA g^{-1})	70/300 (500 mA g^{-1})	16
CuHCF	1 M $ZnSO_4$	0.8–1.9 (1.1)	56 (20 mA g^{-1})	77/20 (20 mA g^{-1})	17
BL-V_2O_5	0.5 M AN-$Zn(TFSI)_2$	0.3–1.5 (1.2)	196 (0.1C)	87/120 (0.1C)	18
V_2O_5	3 M $ZnSO_4$	0.4–1.4 (1)	224 (100 mA g^{-1})	75/400 (2 A g^{-1})	19
LiV_3O_8	1 M $ZnSO_4$	0.6–1.2 (0.6)	267 (15 mA g^{-1})	100/65 (133 mA g^{-1})	20
$Na_{1.1}V_3O_{7.9}$@rGO	1 M $Zn(CF_3SO_3)_2$	0.4–1.4 (1)	191 (50 mA g^{-1})	85/500 (1 A g^{-1})	21
α-$Zn_2V_2O_7$	1 M $ZnSO_4$	0.4–1.4 (1)	190.5 (300 mA g^{-1})	85/1000 (4 A g^{-1})	22
$Na_2V_6O_{16}·3H2O$	1 M $ZnSO_4$	0.4–1.4 (1)	267 (1.8 A g^{-1})	80/1000 (14.44 A g^{-1})	23
$K_2V_6O_{16·2}.7H2O$	1 M $ZnSO_4$	0.4–1.4 (1)	217 (200 mA g^{-1})	82/500 (6 A g^{-1})	24
$K_2V_8O_{21}$	2 M $ZnSO_4$	0.4–1.4 (1)	247 (300 mA g^{-1})	83/300 (6 A g^{-1})	25

$V_{0.91}Al_{0.05}O_{1.52}(OH)_{0.77}$	1 M $ZnSO_4$	0.2–1.13 (0.93)	156 (15 mA g^{-1})	67/50 (15 mA g^{-1})	26
VS_2	1 M $ZnSO_4$	0.4–1.0 (0.6)	190.3 (50 mA g^{-1})	98/200 (0.5 A g^{-1}	27
Mo_6S_8	1 M $ZnSO_4$	0.25–1.0 (0.75)	92 (0.1C)	95/150 (180 mA g^{-1})	28
Quinone	3 M Zn(CF3SO3)2	0.2–1.8 (1.6)	335 (20 mA g^{-1})	87/1000 (0.5 A g^{-1})	29
Tetrachloro-1,4-benzoquinone	1 M Zinc trifluoromethanesulfonate ($Zn(OTf)_2$)	0.8–1.4 (0.6)	200 (0.2C)	70/200 (1C)	30
$FeFe(CN)_6$	1 M ($Zn(OAc)_2$, ([Ch]OAc) (70%)	0.5–1.8 (1.3)	50 (0.1 mA cm^{-2})	98/50 (mA cm^{-2})	31
Co_3O_4	2 M $ZnSO_4$ + 0.2 M $CoSO_4$	0.8–2.2 (1.4)	158 (1 A g^{-1})	92/5000 (4 A g^{-1})	32
$ZnNi_{1/2}Mn^{1/2}CoO_4$	0.3 M $Zn(OTf)_2$ in MeCN	0.9–2.15 (1.25)	180 (0.2C)	83/200 (200)	33
PANI	1M $ZnSO_4$	0.5–1.6 (1.1)	184 mAh g^{-1} (200 mAg^{-1})	70/2000 (10 Ag^{-1})	34

Table S4: The comparison table of **HqTp** COF with reported cathode materials for zinc ion batteries.

Note: To compare the performance of the **HqTp** COF with reported cathode material, we have taken the specific capacity obtained from the overall potential window of the ZIB. Herein, the differences in the voltage plateau in charge-discharge curves of various materials have not been considered for simplifying the comparison. Additionally, we have considered charge-discharge cyclic stability at a particular current rate for analyzing the overall performance of the material.

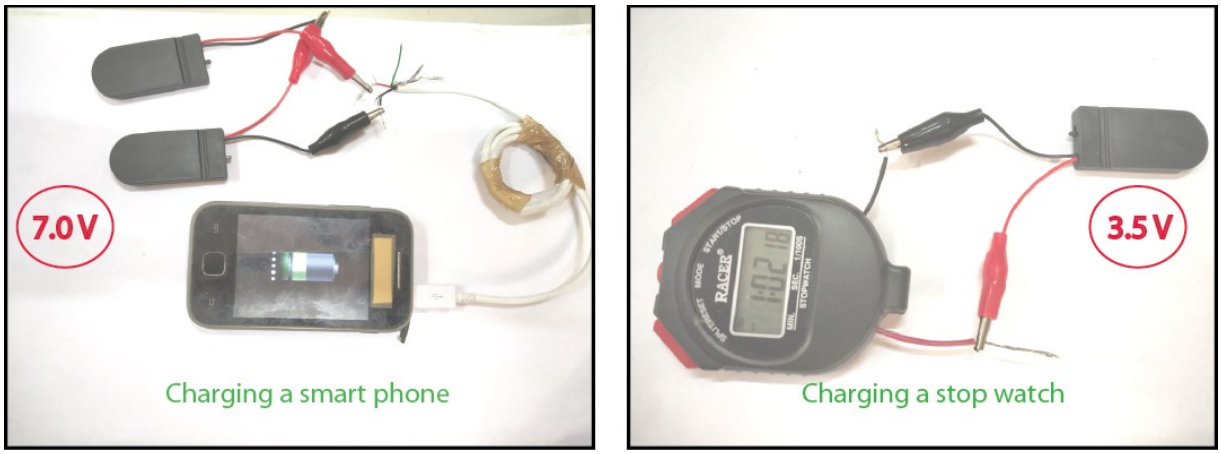

Figure S29: Charging a smart phone and a stop watch.

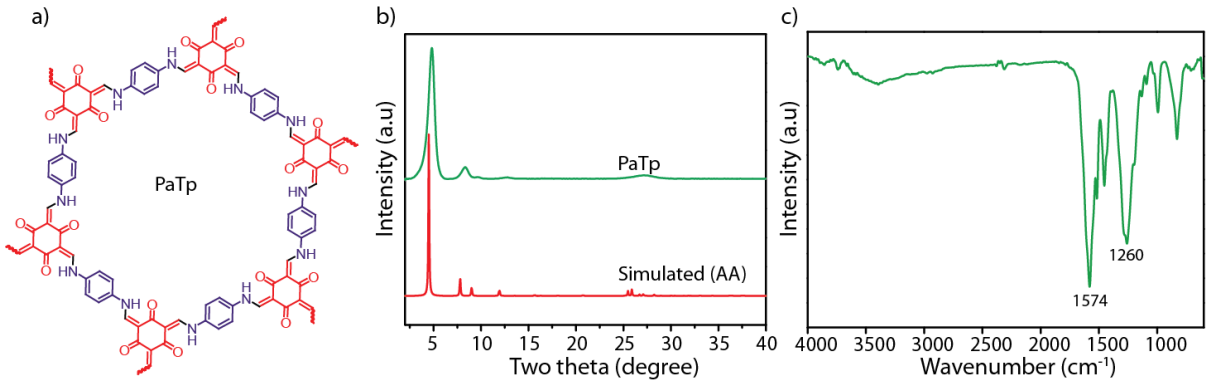

Figure S30: a) **PaTp** COF ; b) PXRD and c) IR of **PaTp** COF.

S-10: References

1. J. H. Chong, M. Sauer, B.O. Patrick, M. J. MacLachlan, *Org. Lett.* **2003**, *5*, 3823

2. R. Kantam, R. Holland, B. P. Khanna, K. D. Revell, *Tetrahedron Lett.***2011**, *52*, 5083

3. E. W. L. Chan, M.N. Yousaf, *J. Am. Chem. Soc***. 2006**, *128*, 15542-15546.

4 C. Gerbaldi, M. Destro, J. R. Nair, S. Ferrari, I. Quinzeni , E. Quartarone, *Nano Energy*, **2013**, *2*, 1279–1286.

5. L. Zhang, L. Chen, X. Zhou, Z. Liu, *Advanced Energy Materials*, **2015**, *5*, 1400930.

6. C. Xu, B. Li, H. Du, F. Kang, *Angew. Chem., Int. Ed*. **2012**, *51*, 933−935.

7. M. H. Alfaruqi, S. Islam, V. Mathew, J. Song, S. Kim, D. P. Tung, J. Jo, S. Kim, J. P. Baboo, Z. Xiu, J. Kim, *Appl. Surf. Sci*. **2017**, *404*, 435−442.

8. M. H. Alfaruqi, J. Gim, S. Kim, J. Song, J. Jo, S. Kim, V. Mathew, J. Kim, *J. Power Sources* **2015**, *288*, 320−327.

9. J. Lee, J. B. Ju, W. I. Cho, B. W. Cho, S. H. Oh, *Electrochim. Acta* **2013**, *112*, 138−143.

10. D. Xu, B. Li, C. Wei, Y. B. He, H. Du, X. Chu, X.Qin, Q. H.Yang, F. Kang, *Electrochim. Acta* **2014**, *133*, 254−261.

11. D. Chao, C. Zhu, M. Song, P. Liang, X. Zhang, N. H. Tiep, H. Zhao, J. Wang, R. Wang, H. Zhang, H. J. Fan. *Adv. Mater*. **2018**, *30*, 1803181.

12. M. Chamoun, W. R. Brant, C. W. Tai, G. Karlsson, D. Noréus, *Energy Storage Mater*. **2018**, *15*, 351−360.

13. S. D. Han, S. Kim, D. Li, V. Petkov, H. D. Yoo, P. J. Phillips, H. Wang, J. J. Kim, K. L. More, B. Key, R.F. Klie, J. Cabana, V. R. Stamenkovic, T. T. Fister, N. M. Markovic, A. K. Burrell, S. Tepavcevic, J. T. Vaughey, *Chem. Mater*. **2017**, *29*, 4874−4884.

14. N. Zhang, F. Cheng, Y. Liu, Q. Zhao, K. Lei, C. Chen, X. Liu, J. Chen, *J. Am. Chem. Soc.* **2016**, *138*, 12894−12901.

15. B. Jiang, C. Xu, C. Wu, L. Dong, J. Li, F. Kang, *Electrochim. Acta* **2017**, *229*, 422−428.

16. J. Hao, J. Mou, J. Zhang, L. Dong, W. Liu, C. Xu, F. Kang, *Electrochim. Acta* **2018**, *259*, 170−178.

17. Z. Jia, B. Wang, Y. Wang, *Mater. Chem. Phys.* **2015**, *149−150*, 601−606.

18. P. Senguttuvan, S. D. Han, S. Kim, A. L. Lipson, S. Tepavcevic, T. T. Fister, I. D. Bloom, A. K. Burrell, C. S. Johnson, *Adv. Energy Mater*. **2016**, *6*, 1600826.

19. J. Zhou, L. Shan, Z. Wu, X. Guo, G. Fang, S. Liang, *Chem. Commun*. **2018**, *54*, 4457−4460.

20. M. H. Alfaruqi, V. Mathew, J. Song, S. Kim, S. Islam, D. T. Pham, J. Jo, S. Kim, J. P. Baboo, Z. Xiu, K.-S. Lee, Y.-K. Sun, J. Kim, *Chem. Mater*. **2017**, *29*, 1684−1694.

21. Y. Cai, F. Liu, Z. Luo, G. Fang, J. Zhou, A. Pan, S. Liang, *Energy Storage Mater.* **2018**, *13*, 168−174.

22. B. Sambandam, V. Soundharrajan, S. Kim, M. H. Alfaruqi, J. Jo, S. Kim, V. Mathew, Y.-K. Sun, J. Kim, *J. Mater. Chem. A* **2018**, *6*, 3850−3856.

23. V. Soundharrajan, B. Sambandam, S. Kim, M. H. Alfaruqi, D. Y. Putro, J. Jo, S. Kim, V. Mathew, Y.-K. Sun, J. Kim, *Nano Lett*. **2018**, *18*, 2402−2410.

24. B. Sambandam, V. Soundharrajan, S. Kim, M. H. Alfaruqi, J. Jo, S. Kim, V. Mathew, Y.-K. Sun, J. Kim, *J. Mater. Chem. A* **2018**, *6*, 15530− 15539.

25. B. Tang, G. Fang, J. Zhou, L. Wang, Y. Lei, C. Wang, T. Lin, Y. Tang, S. Liang, *Nano Energy* **2018**, *51*, 579−587.

26. J. H. Jo, Y.-K. Sun, S.-T. Myung *J. Mater. Chem. A* **2017**, *5*, 8367−8375.

27. P. He, M. Yan, G. Zhang, R. Sun, L. Chen, Q. An, L. Mai, *Adv. Energy Mater.* **2017**, *7*, 1601920.

28. Y. Cheng, L. Luo, L. Zhong, J. Chen, B. Li, W. Wang, S. X. Mao, C. Wang, V. L. Sprenkle,; G. Li, J. Liu, *ACS Appl. Mater. Interfaces* **2016**, *8,* 13673−13677.

29. Q. Zhao, W. Huang, Z. Luo, L. Liu, Y. Lu, Y. Li, L. Li, J. Hu, H. Ma, J. Chen, *Sci. Adv.* **2018**, *4*, eaao1761.

30. D. Kundu, P. Oberholzer, C. Glaros, A. Bouzid, E. Tervoort, A. Pasquarello, M. Niederberger, *Chem. Mater*. **2018**, *30*, 3874−3881

31. S. Zhang, N. Yu, S. Zeng, S. Zhou, M. Chen, J. Di, Q. Li, *J. Mater. Chem. A* **2018**, *6*, 12237−12243.

32. L. Ma, S. Chen, H. Li, Z. Ruan, Z. Tang, Z. Liu, Z. Wang, Y. Huang, Z. Pei, J. A. Zapien, C. Zhi, *Energy Environ. Sci*. **2018**, *11*, 2521.

33. C. Pan, R. Zhang, R. G. Nuzzo, A. A. Gewirth, *Adv. Energy Mater*. **2018**, *8*, 1800589.

34. H.-Y. Shi, Y.-J. Ye, K. Liu, Y. Song, X. Sun, *Angew.Chem.Int.Ed*. **2018**, *57*, 16359–16363.